






Kinetics of phagosome maturation is coupled to their intracellular motility

Yanqi Yu^{1,4}, Zihan Zhang^{1,4} , Glenn F. W. Walpole^{2,3}  & Yan Yu¹  

Immune cells degrade internalized pathogens in phagosomes through sequential biochemical changes. The degradation must be fast enough for effective infection control. The presumption is that each phagosome degrades cargos autonomously with a distinct but stochastic kinetic rate. However, here we show that the degradation kinetics of individual phagosomes is not stochastic but coupled to their intracellular motility. By engineering RotSensors that are optically anisotropic, magnetic responsive, and fluorogenic in response to degradation activities in phagosomes, we monitored cargo degradation kinetics in single phagosomes simultaneously with their translational and rotational dynamics. We show that phagosomes that move faster centripetally are more likely to encounter and fuse with lysosomes, thereby acidifying faster and degrading cargos more efficiently. The degradation rates increase nearly linearly with the translational and rotational velocities of phagosomes. Our results indicate that the centripetal motion of phagosomes functions as a clock for controlling the progression of cargo degradation.

¹Department of Chemistry, Indiana University, Bloomington, IN 47405-7102, USA. ²Program in Cell Biology, The Hospital for Sick Children, Toronto, Ontario, Canada. ³Department of Biochemistry, University of Toronto, Toronto, Ontario, Canada. ⁴These authors contributed equally: Yanqi Yu, Zihan Zhang. email: yy33@iu.edu

Innate immune cells, such as macrophages, ingest pathogens and dead cells via a phagocytosis process. This is an essential process in infection control and tissue homeostasis. After recognizing ligands on pathogens, immune cells internalize them into phagosomes and transport them from the cell periphery to the perinuclear region^{1–5}. During this intracellular transport, phagosomes degrade the entrapped pathogens through sequential biochemical transformations, including the acidification of the lumen⁶, the activation of hydrolytic enzymes⁷, and the generation of reactive oxygen species⁸. The progression of phagosome maturation through the different steps is tightly orchestrated, such that pathogens are degraded efficiently inside phagosomes to prevent persistent infection. However, it is unknown what determines the kinetic rate of cargo degradation in phagosomes. The complexity in addressing this question is that phagosomes do not mature at a unified kinetic rate. Instead, each phagosome matures autonomously with distinct kinetic rates, even for those formed via the same receptor-mediated phagocytosis within the same cell^{9–12}. Because of such individuality of phagosomes, any deterministic factors that regulate the kinetics of phagosome maturation must be studied at the single-phagosome level.

It is known that the degradative function of phagosomes is tightly associated with their cytoskeleton-dependent transport in cells. Many pathogens, such as the bacterium *Legionella pneumophila*, evade the degradative environment in phagosomes by hijacking the intracellular trafficking process^{13–15}. Extensive studies revealed the role of cytoskeleton-based phagosome transport in phagosome maturation by disrupting the cytoskeleton or molecular motor functions with inhibitors. The disruption of actin was shown to attenuate phagosome-endosome fusion^{16–18}. Microtubule depolymerization was found to disrupt: i) phagosome-lysosome fusion¹⁹, ii) content delivery from late endosomes to phagosomes²⁰, and iii) acquisition of lysosome markers²¹. These studies established the qualitative evidence that the active transport of phagosomes in cells is required for their acquisition of maturation machineries and degradative capacities. However, the population-based measurements used in those studies neglected the individuality of phagosome functions. Each phagosome matures at distinct kinetic rates. They also move on actin or microtubules at distinct velocities, as revealed by single-particle imaging and tracking studies^{22,23}. The transport velocity and maturation kinetic rate of phagosomes were each presumably randomly distributed. However, is there any quantitative relationship between the two parameters? Specifically, because phagosomes must move on microtubules to fuse with endosomes and lysosomes, does the kinetics of phagosome maturation depend on the transport velocity?

To address this question, here we develop a single-phagosome imaging toolset for monitoring both maturation kinetics and dynamics of individual phagosomes. The RotSensor particles are optically anisotropic and fluorogenic in response to acidification in phagosomes and phagosome-lysosome fusion, two key degradative activities. Using the RotSensors as cargos in phagosomes, we imaged simultaneously the biochemical changes during phagosome maturation and their translational and rotational dynamics in living cells. By combining this toolset with magnetic tweezers to control the dynamics of phagosomes, we obtained direct evidence that the microtubule-based centripetal transport of phagosomes determines the kinetic rates of their maturation process. More mobile phagosomes fuse with lysosomes and acidify in their lumen more rapidly, following a nearly linear relationship. Our results reveal the orchestration of the dynamical and biochemical processes that occur during pathogen degradation in phagosomes, providing a possible mechanism by which some pathogens may evade immune clearance by disrupting the intracellular dynamics of residing phagosomes.

Results

pH-responsive rotational particle sensors (pH-RotSensors) for measuring phagosome acidification and dynamics. The acidification of phagosome lumen is an early indicator of its degradative function and is required for many subsequent events, including the activation of degradative enzymes^{24,25}. Therefore, we first designed pH-responsive RotSensors to simultaneously measure the acidification of single phagosomes and their intracellular transport dynamics, including both translational and rotational movements (Fig. 1a). Each RotSensor consists of a pH-responsive particle (1 μm diameter) covalently conjugated with a smaller green particle (100 nm diameter) with nonoverlapping fluorescence emission (Fig. 1b). Once engulfed into phagosomes, the “snowman”-like RotSensors report both the translational and the rotational motion of the residing phagosome. The azimuthal (φ) and polar (θ) angles of each RotSensor can be measured, respectively, from the orientation and projection distance between the pair of the two particles (Fig. 1b)²⁶.

To monitor phagosome acidification, the 1 μm particle in each RotSensor was biotinylated and subsequently conjugated with two types of streptavidin, one type labeled with the pH-indicator pHrodo Red and the other with the reference dye CF640R. The dye pHrodo Red fluoresces intensely in an acidic environment. pHrodoRed fluorescence is sensitive to NADPH oxidase (NOX2) activity⁸ but this is not an issue here as NOX2 activity is not manipulated in the experiments. CF640R was chosen as a reference dye because it is pH insensitive and photostable (Supplementary Fig. 1). Streptavidin is critical in the RotSensor design because it acts as a cushion layer to separate the pHrodo Red dye from the particle surface. Without the streptavidin linker, pHrodo Red that was directly conjugated onto the particle surface exhibited little pH sensitivity. The pH-sensitive RotSensors were then coated with immunoglobulin G (IgG) via nonspecific adsorption to initiate Fc receptor-dependent phagocytosis in RAW264.7 macrophage cells. The adsorption of IgG on RotSensors was confirmed by the presence of fluorescently labeled IgG on the particles in microscopy images (Supplementary Fig. 2).

To quantify the pH response of the RotSensors, we measured the ratio of fluorescence emission intensities of pHrodo Red and of the reference dye CF640R; $I_{\text{pHrodo}}/I_{\text{ref}}$ as we varied pH inside phagosomes in live cells and in aqueous buffers (Supplementary Fig. 3). For both cases, $I_{\text{pHrodo}}/I_{\text{ref}}$ of the RotSensors increased linearly with decreasing pH, consistent with previous reports²⁷. The pH responses of individual RotSensors, including the initial $I_{\text{pHrodo}}/I_{\text{ref}}$ ratio and slope, varied slightly from one to another, because of the different amounts of dyes on particles and the slightly different phagosome lumen environments^{28–31}. To eliminate the effect of such variation in pH measurements, we calibrated our pH measurements for each phagosome. We measured $I_{\text{pHrodo}}/I_{\text{ref}}$ of each phagosome versus time and then converted the intensity ratio to pH based on $I_{\text{pHrodo}}/I_{\text{ref}}$ of the same phagosome at pH 4.5 and 7.3 (details in Methods section).

pH-RotSensors reveal correlation between phagosome acidification rate and transport dynamics. Before tracking the dynamics of phagosomes, we first asked whether the rotation of RotSensors faithfully reports the rotation of their residing phagosomes. Transmission electron microscopy (TEM) images show that $\approx 86\%$ of internalized RotSensors remained tightly wrapped by the phagosome membrane at the end of our experiments (50 min after particles were added to cells) (Supplementary Fig. 4). Based on the tight membrane fitting and the presence of ligand-receptor binding between the RotSensors and phagosome

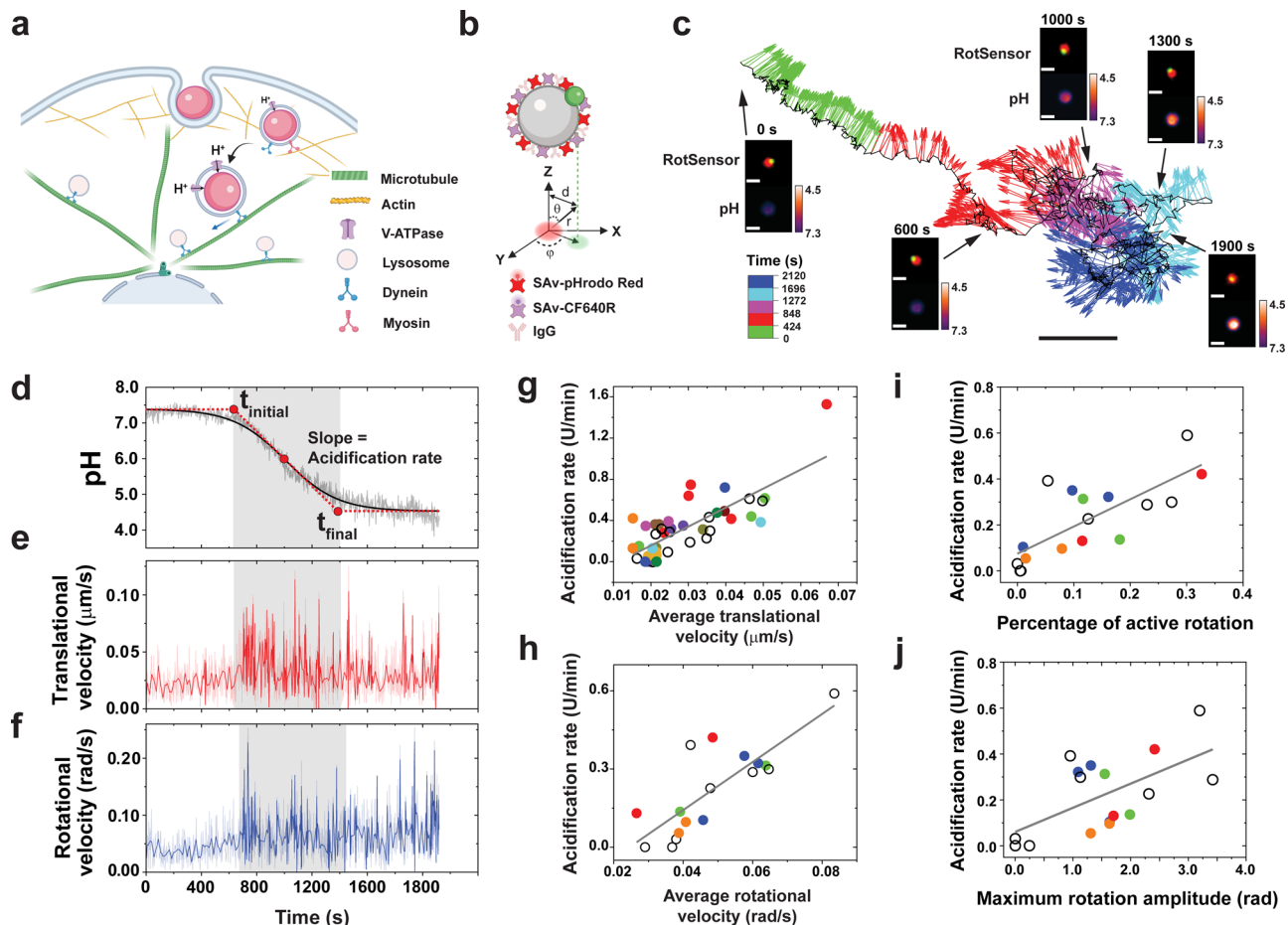


Fig. 1 Simultaneous measurement of phagosome dynamics and acidification. **a** Schematics showing internalization of pH-sensitive RotSensors into phagosomes in macrophage cells. **b** Schematic illustration of the RotSensor design. Each RotSensor contains a 1 μm silica particle tethered with a 100 nm yellow-green fluorescent particle. The silica particles were coated with streptavidin (SAv)-pHrodo Red (pH reporter) and SAv-CF640R (reference). The azimuthal (φ) and polar (θ) angles of each pH-RotSensor were analyzed based on its projection fluorescence image. **c** A representative trajectory of a pH-RotSensor-containing phagosome. Vectors indicate the orientation of the pH-RotSensor and are color-coded based on time. Scale bar, 2 μm . Insets show fluorescence images of the RotSensor (top) and the pH response (bottom). Scale bar, 1 μm . Line plots showing acidification (**d**), translational velocities (**e**) and rotational velocities (**f**) of the pH-RotSensor-containing phagosome in **c**. The acidification profile is fitted with sigmoidal function to determine the initial pH, final pH, the period of rapid acidification (t_{initial} to t_{final}), and acidification rate. The period of rapid acidification is highlighted in gray. Darker lines in **e** and **f** are velocity values after wavelet denoising. Scattered plots showing acidification rates against translational (**g**) and rotational velocities (**h**) of single phagosomes. Each data point represents one single phagosome. Data points from multiple phagosomes within the same cells are shown in the same solid color. Data points from cells containing only one phagosome are shown as black circles. $N = 42$ phagosomes from 24 cells for translational tracking, and 17 phagosomes from 12 cells for rotational tracking. Pearson's coefficients of 0.78 and 0.81 were obtained in **g** and **h**, respectively. Scatter plots showing acidification rates against percentage of active rotation (**i**) and maximum rotation amplitude (**j**) of single phagosomes during rapid acidification period. $N = 17$ phagosomes from 12 cells. Pearson's coefficients of 0.76 and 0.61 are obtained in **i** and **j**.

membranes, the RotSensors are unlikely to freely rotate inside phagosomes. Thus, their rotation is expected to report the rotation of their residing phagosomes.

We then simultaneously imaged the pH response and the rotational and translational dynamics of single phagosomes encapsulating RotSensors in RAW264.7 macrophage cells activated with a combination of lipopolysaccharides (LPS) and interferon-gamma ($\text{IFN-}\gamma$) (Fig. 1c). Phagosomes acidified in three steps: 1) an initial standby period during which the phagosome pH remained at neutral pH of ≈ 7.3 (Fig. 1d), 2) a rapid acidification period when the pH quickly dropped over a period of a few minutes, and 3) an eventually plateau at pH 4.5–5.0. This acidic pH is a prerequisite for activating degradative enzymes^{8,32}. While individual phagosomes reached slightly different final pH values, their acidification kinetics mostly (31

of 42 phagosomes) followed a sigmoidal function:

$$\text{pH} = \text{pH}_{\text{final}} + \frac{\text{pH}_{\text{initial}} - \text{pH}_{\text{final}}}{1 + \exp\left(\frac{t-t_0}{dt}\right)} \quad (1)$$

in which t_0 is the half-response point, and t_{initial} and t_{final} denote the beginning and the end of rapid acidification, respectively (Fig. 1d). Slope at t_0 is the acidification rate by definition. We found that phagosomes acidified at an average rate of 0.33 ± 0.28 pH unit/min ($N = 42$). The acidification of phagosomes requires intact microtubules, as the acidification was abolished upon microtubule disruption by nocodazole (Supplementary Fig. 5). In all experiments, we confirmed the internalization of RotSensors using a trypan blue assay (see Methods).

For transport dynamics, we observed that a majority (~70%) of phagosomes exhibited a slow-to-fast movement transition both translationally and rotationally (Fig. 1e, f). The remaining 30% of phagosomes exhibited only slow movements. These initially slow movements are not dependent on microtubules, as the average velocities were not affected by microtubule depolymerization (Supplementary Fig. 6). After a few minutes of slow movements, phagosomes rapidly moved centripetally with velocities up to 0.1 $\mu\text{m/s}$ (Fig. 1e). This range of phagosome velocities is consistent with literature reports for 1 μm bead-containing phagosomes in macrophage cells²². Meanwhile, phagosomes also rotated frequently in between segments of translational motion with rotational velocities up to 0.15 rad/s (Fig. 1f). These dynamic behaviors, particularly phagosome rotation, are characteristic of cargo transport driven by microtubule-based molecular motors³³. This was further confirmed in control experiments, in which the rapid translational and rotational dynamics disappeared in cells treated with nocodazole (Supplementary Fig. 6).

Notably, the beginning of the rapid acidification period appeared to coincide with the onset of fast microtubule-based transport (Fig. 1e, f). To explore the possible correlation between the two processes, we calculated the acidification rate of single phagosomes based on the sigmoidal fitting of their individual pH-time plots (Fig. 1d). We then plotted the acidification rate of single phagosomes against their individual translational and rotational velocities during the rapid acidification phase (from t_{initial} to t_{final}) (Fig. 1g, h). The acidification rate varied broadly among phagosomes, even those from the same cells. This reflected the individuality of each phagosome in maturation. Despite this heterogeneity, the acidification rates of individual phagosomes follow a linear relationship with both their translational and rotational velocities with a Pearson's coefficient of 0.78 and 0.81, respectively. Those observations apply not only to phagosomes from different cells but also to those from the same cells. This is shown in Fig. 1g, h, in which data of phagosomes from the same cells are the same color. This is also a general phenomenon independent of the activation status of macrophage cells (Supplementary Fig. 7).

Further, the acidification rates of single phagosomes also follow a linear relationship with the percentage, maximum amplitude, and frequency of active rotation of phagosomes during the rapid acidification phase (from t_{initial} to t_{final}) with a Pearson's coefficient of 0.76, 0.60, and 0.61, respectively (Fig. 1i, j, and Supplementary Fig. 8). For this analysis, active rotation of phagosomes was distinguished from passive random rotation by using a Wavelet analysis method reported previously (Supplementary Fig. 9; Methods)³⁴. The percentage of active rotation was defined as the total time during which the phagosome underwent active rotation divided by the time duration of its rapid acidification (from t_{initial} to t_{final}). The results altogether indicate that more mobile phagosomes acidify faster. As additional evidence supporting this conclusion, we also observed that the ~30% of phagosomes that never underwent rapid microtubule-based transport exhibited minimal acidification (Supplementary Fig. 10a–c). Surprisingly, the final pH of individual phagosomes showed no correlation with either their transport dynamics (i.e., translational and rotational velocities) or their acidification rate (Supplementary Fig. 11). Because the final acidic pH determines whether a phagosome can successfully degrade its cargo, this result suggests that the degradative capacity of a phagosome is likely determined prior to its transport on microtubules, but that the rate of degradation is correlated with the transport dynamics.

FRET-RotSensors for measuring phagosome-lysosome fusion. During cargo degradation, phagosome acidification relies on its

continuous fusion with lysosomes, which deliver proton-pumping vacuolar H⁺-ATPase (V-ATPase) to it^{30,35–38}. Since we found that more mobile phagosomes acidify more rapidly, we asked whether phagosome-lysosome fusion is likewise correlated with phagosome mobility. To do this, we measured the kinetics of phagosome-lysosome fusion by modifying the RotSensor design into a Förster Resonance Energy Transfer (FRET)-based assay, using a similar experimental design as previously reported^{32,39}. This fluorescence assay can be used to determine when two fluorophores, a donor inside phagosomes and an acceptor inside lysosomes, are in close proximity to one another. FRET-sensitive RotSensors were prepared in the same way as pH-sensitive RotSensors, but, in this case, the sensor particles were labeled with streptavidin that was conjugated with the donor fluorophore Alexa568 (Fig. 2a). For FRET, lysosomes were loaded with fluid-phase biotinylated bovine serum albumin (BSA) that was conjugated with the acceptor fluorophore Alexa647 using a pulse-chase procedure⁴⁰. We confirmed that the BSA-Alexa647-biotin was contained inside lysosomes based on its colocalization with the lysosome marker LysoTracker inside cells (Supplementary Fig. 12). Inside lysosomes, BSA-Alexa647-biotin was fragmented by proteases before RotSensors were added to cells for internalization (Supplementary Fig. 13). The working principle of the FRET assay is that once the contents of lysosomes are intermixed with the phagosome lumen during fusion, the fragmented BSA-Alexa647-biotin from lysosomes will be in close proximity with Alexa568 conjugated RotSensors, then induces FRET effect. The magnitude of the FRET signal thus indicates the extent of phagosome-lysosome fusion. This assay does not necessarily require biotin–streptavidin binding. We showed in *in vitro* experiments that FRET can occur when BSA-Alexa647, without biotinylation, was added to FRET-RotSensors in 1 \times PBS solution (Supplementary Fig. 14). However, we still used BSA-Alexa647-biotin in this FRET assay because it was loaded into lysosomes much more efficiently than BSA-Alexa647 alone, which improved the sensitivity of the FRET assay (Supplementary Fig. 15). The observation that the biotin moiety promotes uptake of BSA by cells is consistent with previous reports^{41,42}, and might be because biotinylation alters the endocytic pathway of BSA by physically masking the protein surface. For the FRET assay to accurately detect continuous fusion of a phagosome with lysosomes, the concentration of acceptor fluorophores (Alexa647) loaded into lysosomes must be optimized to achieve sufficient FRET efficiency without saturating the donor on the RotSensors. We did this by optimizing the loading concentration of BSA-Alexa647-biotin into lysosomes (see Methods).

We next tested and optimized the FRET assay in live cells. To start with, we loaded lysosomes using 10 $\mu\text{g/ml}$ BSA-Alexa647-biotin ($[\text{BSA-Alexa647-biotin}]_{\text{loading}} = 10 \mu\text{g/ml}$). After internalization of FRET-RotSensors, the FRET-RotSensors inside phagosomes exhibited decreased fluorescence emission in the donor channel (ex/em: 561/586 nm) and simultaneously increased emission in FRET channel (ex/em: 561/680 nm) (Fig. 2b, c). For quantification, we calculated FRET ratio defined as:

$$\text{FRET ratio} = \frac{\text{FRET}_{em}}{\text{AF568}_{em}} = \frac{\text{FRET}_0 - \alpha \times \text{AF568}_{em} - \beta \times \text{AF647}_{em}}{\text{AF568}_{em}} \quad (2)$$

In this equation, FRET_0 is the measured FRET signal (ex/em 561/680 nm) before correction for spectral bleed-through, AF568_{em} is the emission in the donor channel (ex/em 561/586 nm), and AF647_{em} is the emission in the acceptor channel (ex/em 660/680 nm). The coefficient α corrects the bleed-through contribution from the donor (Alexa568) due to the overlap of the donor emission in the FRET channel. The coefficient β corrects

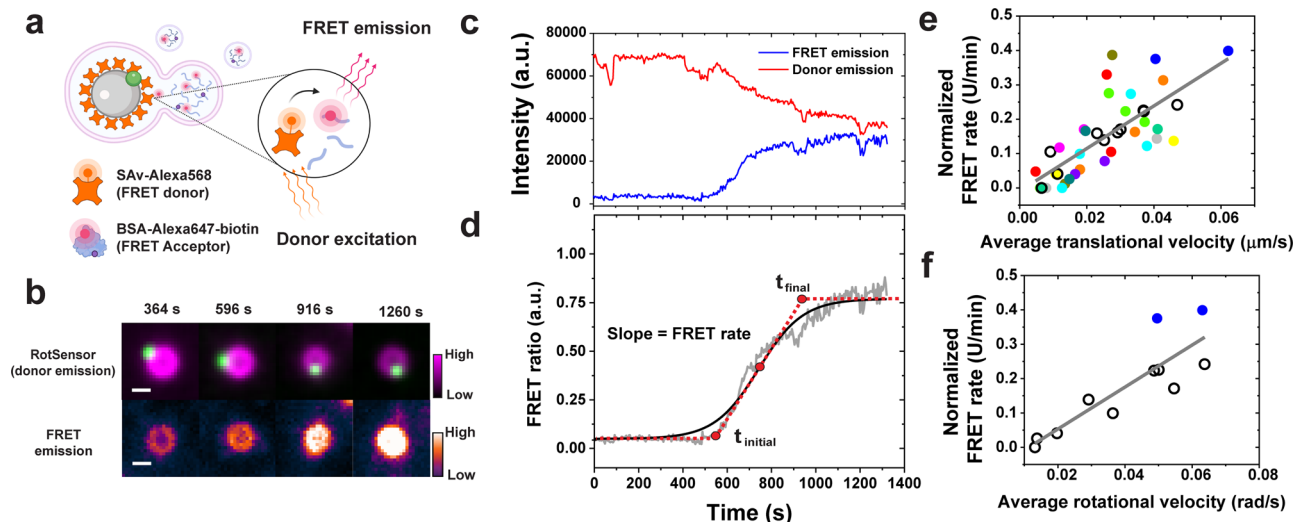


Fig. 2 Simultaneous measurement of phagosome-lysosome fusion and phagosome transport dynamics. **a** Schematic illustration of the Förster resonance energy transfer (FRET)-based phagosome-lysosome fusion assay. The FRET-RotSensor was coated with SA-Alexa568 (FRET donor). BSA-Alexa647-biotin (FRET acceptor) was loaded into lysosomes. Phagosome fusion with lysosomes leads to intermixing between donor fluorophore (Alexa568) and fluid phase acceptor fluorophore (Alexa647) generating FRET emission (680 nm) under the donor excitation of 561 nm. **b** and **c** Fluorescence images and intensity plots showing the change of FRET emission (ex/em: 561/680 nm) and donor emission (magenta, ex/em: 561/586 nm) from a FRET-RotSensor (100 nm yellow-green nanoparticle in green) in a RAW264.7 macrophage. Scale bar, 2 μm . **d** FRET ratio vs. time plot is fitted with sigmoidal function (shown as the black solid line) to determine the initial time point of phagosome-lysosome fusion (t_{initial}), the time point where FRET-signal reaches a plateau (t_{final}), and the FRET rate, as indicated by the red dotted line. Scatter plots showing normalized FRET rate against translational velocity (**e**) and rotational velocities (**f**) of single phagosomes during the period of its fusion with lysosomes. Each data point represents data from a single phagosome. Data points from multiple phagosomes within the same cells are shown in the same solid color. Data points from cells containing only one phagosome are shown as black circles. For translational tracking, $N = 40$ phagosomes from 22 cells. For rotational tracking, $N = 11$ phagosomes from 10 cells. The black lines indicate linear regression with a Pearson's coefficient of 0.75 in **e** and of 0.86 in **f**.

the non-FRET bleed-through from the acceptor (Alexa647) due to the excitation of the acceptor at the donor excitation wavelength. Correction factors α and β were determined independently for each experiment (see Methods). After internalization, the FRET ratio of single phagosomes increased continuously with time until it reached a plateau, following a sigmoidal relationship (Fig. 2d). This is a general phenomenon confirmed in over 40 phagosomes from 22. The gradual increase in FRET ratio as a function of time indicates an increasing concentration of acceptors (Alexa647) in phagosomes resulted from their continuous fusion with lysosomes. FRET signal was diminished when microtubules were disrupted by nocodazole treatment, which further confirms that this assay measures phagosome-lysosome fusion (Supplementary Fig. 16).

We then asked: what caused the plateau in the FRET ratio of single phagosomes? There are two possible causes. One is that the concentration of acceptor fluorophores delivered into phagosomes by lysosome fusion reached the threshold needed to saturate the donor fluorophores on RotSensors. The second is that the acceptor concentration in the phagosome had reached equilibrium with that in the lysosomes that were fusing with it. Even as more lysosomes continued to fuse with the phagosome, the content exchange would no longer increase the concentration of acceptors in the phagosome. To determine which of these two possible circumstances caused the FRET ratio to plateau, we varied $[\text{BSA-Alexa647-biotin}]_{\text{loading}}$ from 2.5 $\mu\text{g/ml}$ to 25 $\mu\text{g/ml}$ (note: concentrations higher than 25 $\mu\text{g/ml}$ resulted in decreased cell viability). While the exact concentration of acceptors (Alexa647) inside lysosomes is unknown, it is proportional to $[\text{BSA-Alexa647-biotin}]_{\text{loading}}$ (Supplementary Fig. 15 and Supplementary Fig. 17a–c). The rationale here is that if the plateau in FRET ratio was caused by the saturation of donors on RotSensors, the magnitude of plateau would be determined by the amount of

donors on RotSensors and thus should not change with $[\text{BSA-Alexa647-biotin}]_{\text{loading}}$. On the contrary, if the plateau of FRET ratio occurred because the acceptor concentration reached an equilibrium between the phagosome and fusing lysosomes, the magnitude of plateau would be determined by the acceptor concentration inside lysosomes and thus should increase with $[\text{BSA-Alexa647-biotin}]_{\text{loading}}$. In experiments, we found that the plateau level of FRET ratio increased with $[\text{BSA-Alexa647-biotin}]_{\text{loading}}$ from 2.5 to 25 $\mu\text{g/ml}$ (Supplementary Fig. 17a–d). This indicates that the FRET ratio plateau was due to the establishment of equilibrium between the phagosome lumen and lysosomes, and not saturation of donors on RotSensors. Based on those results, we further determined that $[\text{BSA-Alexa647-biotin}]_{\text{loading}} = 10 \mu\text{g/ml}$ is an optimal concentration to minimize cell-to-cell variation in loading BSA-Alexa647-biotin into lysosomes (See Methods).

FRET-RotSensors reveal correlation between phagosome-lysosome fusion kinetics and phagosomes centripetal transport. After the validation and calibration of the FRET fusion assay, we then investigated whether the kinetics of phagosome-lysosome fusion (measured as the FRET rate) correlates with the motility of phagosomes. Much like the heterogeneity in acidification, the FRET rate differed greatly between phagosomes even within the same cell (Fig. 2e, f). However, all single phagosome FRET ratio data follow a linear correlation with the translational and rotational velocities of phagosomes, with a Pearson's coefficient of 0.75 and 0.86, respectively (Fig. 2e, f). This indicates that phagosomes that moved faster translationally and rotated more along microtubules also fused more rapidly with lysosomes.

Because lysosomes in macrophages are more concentrated in the perinuclear region (Fig. 3a)⁴³, we then asked if, besides

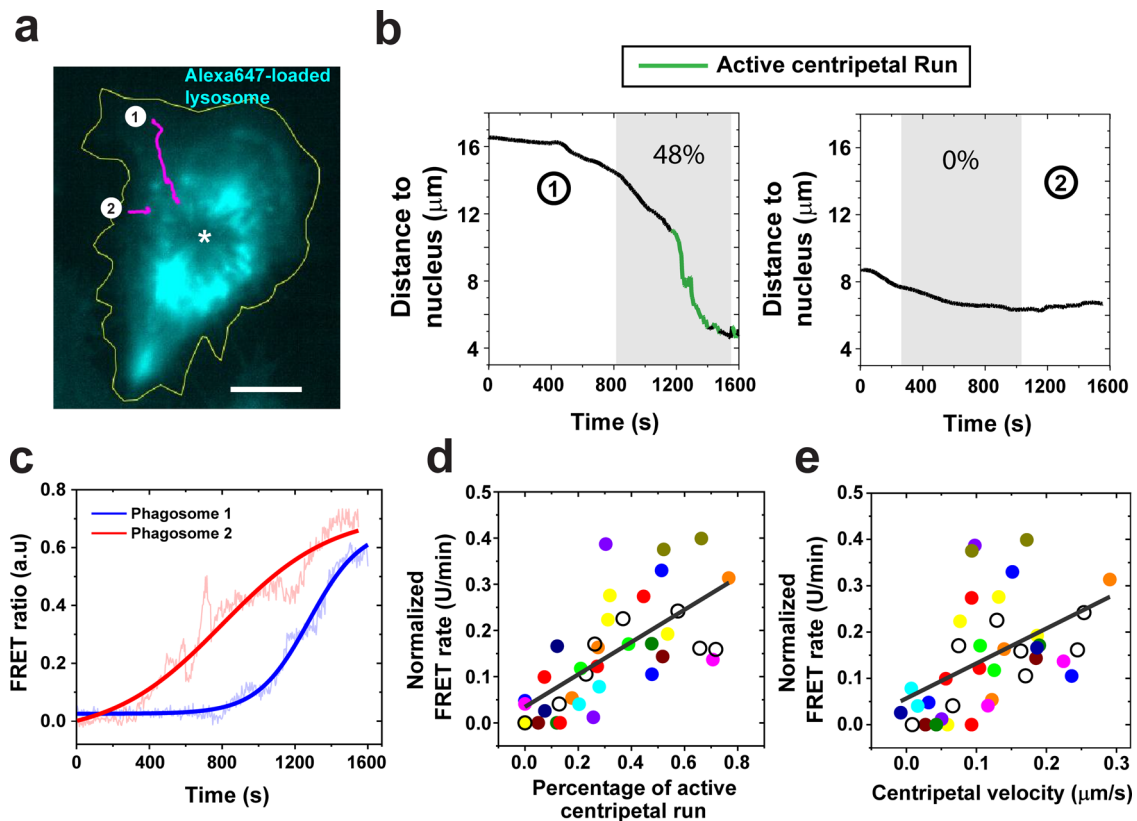


Fig. 3 Correlation of phagosome-lysosome fusion kinetics with the centripetal motility of phagosomes. **a** Fluorescence image showing a cell in which lysosomes were labeled with BSA-Alexa647-biotin. Yellow line indicates the cell periphery, and the asterisk indicates the centroid of the nucleus. The initial positions of two representative phagosomes were indicated by the two number-labeled white dots and their trajectories are shown in magenta. Scale bar, 10 μm . **b** Plots showing the phagosome-to-nucleus distance as a function of time for both the phagosomes indicated in **a**. Segments of active centripetal runs are highlighted in green. Gray shaded area indicates the effective transport distance of the phagosome from the time where it begins to fuse with lysosomes to the time when it reaches the nucleus boundary. The starting time of phagosome lysosome fusion was obtained based on sigmoidal fitting the FRET ratio vs. time plot. Phagosome #1 underwent active centripetal runs in 48% of the time during effective transport, whereas phagosome #2 had no active centripetal run. **c** FRET ratio vs. time plots for both phagosomes marked in **a**. Solid lines indicate sigmoidal fitting to the data. Scatter plots showing normalized FRET rate of single phagosomes plotted against the percentage of active centripetal motion (**d**) and centripetal velocity (**e**). Each data point represents data from a single phagosome. Data from multiple phagosomes inside the same cell are shown in the same solid color. Data from cells in which only one phagosome was studied are shown as black circles. $N = 40$ phagosomes from 22 cells. The black lines indicate linear regression with a Pearson's coefficient of 0.68 and 0.49, respectively.

velocity, the direction of phagosome transport plays any role in their fusion with lysosomes. To identify centripetal transport toward cell nucleus, we analyzed the distance of each phagosome from the center of cell nucleus as a function of time (Fig. 3b). The effective transport distance of a phagosome (gray shaded areas in Fig. 3b) is the distance from the time when it begins to fuse with lysosomes to the time when it reaches the nucleus boundary. The starting time of phagosome-lysosome fusion was obtained from the sigmoidal fitting of the FRET ratio vs. time plot (Fig. 2d). We also identified segments of active centripetal motion following a previously reported method (Fig. 3b)²². Most phagosomes moved centripetally (Supplementary Fig. 18), but not all of them exhibited active centripetal runs (Fig. 3b). As shown in Fig. 3a, phagosome #1 underwent a few segments of active centripetal runs, but phagosome #2 did not. Concurrently, phagosome #1 also fused with lysosomes more rapidly (Fig. 3c). To confirm the generality of this result, we quantified the centripetal velocity and percentage of active centripetal runs of single phagosomes. Centripetal velocity was calculated as the effective transport distance divided by time. The percentage of active centripetal runs was calculated as the sum of the time of all active centripetal runs divided by the total duration of the effective

transport ($N = 40$ phagosomes from 22 cells). The results demonstrate that phagosomes with larger centripetal velocity and higher percentage of active centripetal movements fuse faster with lysosomes (Fig. 3d, e). Because the centripetal transport of phagosomes also changes their subcellular location, we also plotted the phagosome-lysosome fusion rates of single phagosomes as a function of their subcellular location, which was quantified as distance-to-nucleus. For each phagosome, we measured the distance from their location at the end of the centripetal transport to the cell nucleus. To compare results from different cells, we normalized the distance-to-nucleus of single phagosomes by the distance from the cell periphery to the cell nucleus (Supplementary Fig. 19a). The phagosome-lysosome fusion rate (FRET rate) of single phagosomes was plotted with their normalized distance-to-nucleus (Supplementary Fig. 19b). We found that phagosomes that reached closer to the perinuclear region at the end of their transport overall fused faster with lysosomes. Those phagosomes also tend to have larger centripetal velocities. Data points in Supplementary Fig. 19b have a broad distribution, possibly because when we estimated the distance-to-nucleus of phagosomes in 2D projection fluorescence images, some phagosomes may appear closer to the nucleus than the actual situation in 3D. This may

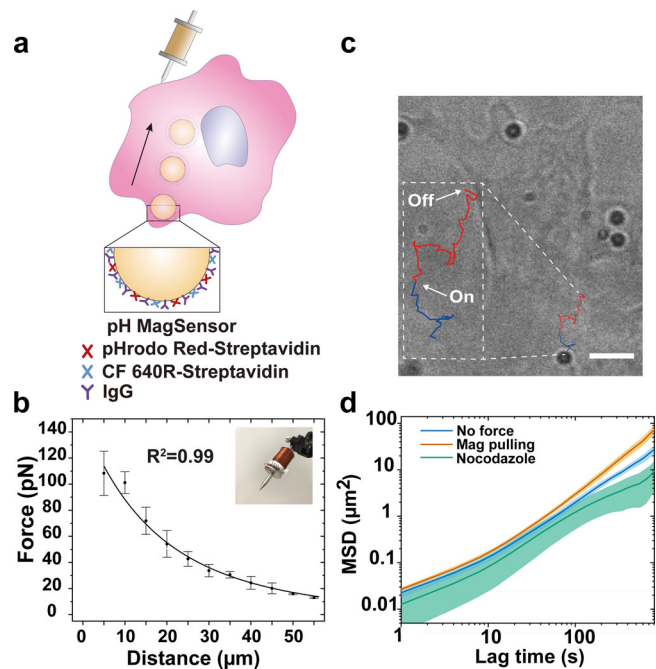


Fig. 4 Phagosome degradation measurements during magnetically manipulated transport. **a** Schematic illustration of the experimental setup. The magnetic gradient is generated by a homemade magnetic tweezers setup built on an inverted fluorescence microscope system. Magnetic pulling force was applied on MagSensors after their internalization into phagosomes. The 1 μm MagSensors were coated with SAv-pHrodo Red (pH indicator), SAv-CF640 (reference), and physically adsorbed IgG. **b** Calibration plot showing the magnetic force exerted on each MagSensor as a function of its distance to the tip of the magnetic tweezers solenoid (shown in inset). Error bars are standard deviations from 5 samples. **c** Bright-field image of a cell overlaid with the trajectory of a MagSensor-containing phagosome under magnetic pulling. The start and end time points of the exertion of magnetic force are indicated. The blue-colored segment of the trajectory indicates the movement of the MagSensor before cell entry; the red-colored segment of the trajectory indicates the intracellular movement of a MagSensor-containing phagosome under magnetic manipulation. Scale bar, 5 μm . **d** Mean-square displacements (MSD) calculated from trajectories of individual MagSensors under different conditions as indicated. Each line is an average of results from $N = 10$ phagosomes from 8 cells (no force), 9 cells (magnetic pulling), and 7 cells (nocodazole). Shaded areas indicate standard deviation of the mean.

explain why a small fraction of phagosomes (6/40) exhibited low phagosome-lysosome fusion rates even though they appeared to be near the perinuclear region in 2D images.

MagSensors for magnetic manipulation and imaging of phagosomes. To determine whether the centripetal motility of phagosomes determines their fusion with lysosomes and consequently their acidification, we applied magnetic tweezers to manipulate the intracellular transport of single phagosomes. We simultaneously measured changes in phagosome acidification (Supplementary Fig. 20). We designed 1 μm magnetically modulated phagosome sensors (MagSensors) that were also pH-responsive (Fig. 4a). The MagSensors were biotinylated and conjugated with SAv-pHrodo Red (pH indicator) and SAv-CF640 (reference), using the same procedure as for the preparation of RotSensors. The MagSensors exhibited similar pH responses (Supplementary Fig. 21). In all experiments, a solenoid tip was positioned on the opposite side of the cell from the phagosome of interest, so that the phagosome could be pulled by magnetic

attraction from the cell periphery towards the center. The magnetic force changes with the distance between the MagSensor and the solenoid tip following theoretical predictions (Fig. 4b, detailed calibration in Methods)⁴⁴. On average, the solenoid tip was positioned $\approx 43 \mu\text{m}$ from the MagSensor of interest. This means that the average force exerted on a MagSensor by the tip was $\approx 21 \text{ pN}$ at the beginning of manipulation and reached as high as $\approx 31 \text{ pN}$ as it moved closer to the tip at the end of imaging (Supplementary Fig. 22).

We performed the magnetic experiments in resting macrophages stably expressing actin-GFP (Supplementary Fig. 23). The fluorescence from actin-GFP allowed us to identify when phagosome formation completes^{45,46}, so that we can apply magnetic pulling force on the MagSensor-containing phagosomes only after their internalization. We used resting cells for these experiments because they are less flat, which allows for better magnetic manipulation of the phagosome. The acidification-motility correlation of phagosomes in resting cells was similar to that in activated cells (Supplementary Fig. 7). In the experiments, we turned on the magnetic force immediately after the MagSensors were internalized into phagosomes, which was indicated by the actin-GFP intensity peak, and pulled the MagSensor-containing phagosomes from the cell periphery towards the center (Fig. 4a). The magnetic force remained on throughout imaging. Under the magnetic pulling force, phagosomes moved towards the magnetic tip with accelerated translational velocity and larger mean square displacements (Fig. 4d and Supplementary Fig. 24). Their trajectories were zigzagged (Fig. 4c), likely because the magnetic force applied on the MagSensors was only slightly larger than the collective forces from the microtubule-based molecular motors. As mentioned above, the magnetic pulling force on single MagSensors was $\approx 21\text{--}31 \text{ pN}$ (Supplementary Fig. 22). For comparison, microtubule-based molecular motors were shown to exert collective forces as high as $\approx 20 \text{ pN}$ on vacuoles encapsulating 1 μm particles⁴⁷. Therefore, the zigzagged movements of phagosomes are plausibly a result of the combined influence of the magnetic force and the forces exerted by molecular motors. We further confirmed that the pulling force generated by magnetic tweezers did not affect cell adhesion, cytoskeleton organization, and lysosome distribution in cells (Supplementary Fig. 25). As the translational velocity of phagosomes accelerated under magnetic pulling, they also acidified more rapidly (Fig. 5a). Phagosomes that were magnetically pulled acidified at an average rate of $0.79 \pm 0.54 \text{ pH unit/min}$ ($N = 38$). In contrast, for phagosomes not subject to magnetic pulling, an average rate of $0.48 \pm 0.34 \text{ pH unit/min}$ was observed ($N = 33$) (Fig. 5b). Surprisingly, magnetic manipulation had no effect on the final pH of the phagosomes, as phagosomes with or without magnetic manipulation reached an average final pH of 4.7 ± 0.4 and 4.7 ± 0.3 , respectively (Fig. 5c). These observations of phagosome acidification were not affected by the number of phagosomes per macrophage cell (Supplementary Fig. 26). In control experiments, we also tested if the centripetal transport of phagosomes is required for productive phagosome maturation. We applied magnetic force immediately after phagosome formation to prevent their centripetal transport towards the cell nucleus. As a result, phagosomes remained near the cell periphery under magnetic force. We found that those phagosomes acidified more slowly ($0.26 \pm 0.21 \text{ pH unit/min}$, $N = 11$) and had a higher average final pH (5.3 ± 0.8 , $N = 11$), compared to phagosomes under no magnetic force (Supplementary Fig. 27). These results together demonstrate that faster centripetal transport of phagosomes leads to faster acidification and more productive maturation.

We next investigated how magnetic pulling affects phagosome-lysosome fusion using the FRET fusion assay shown in Fig. 2.

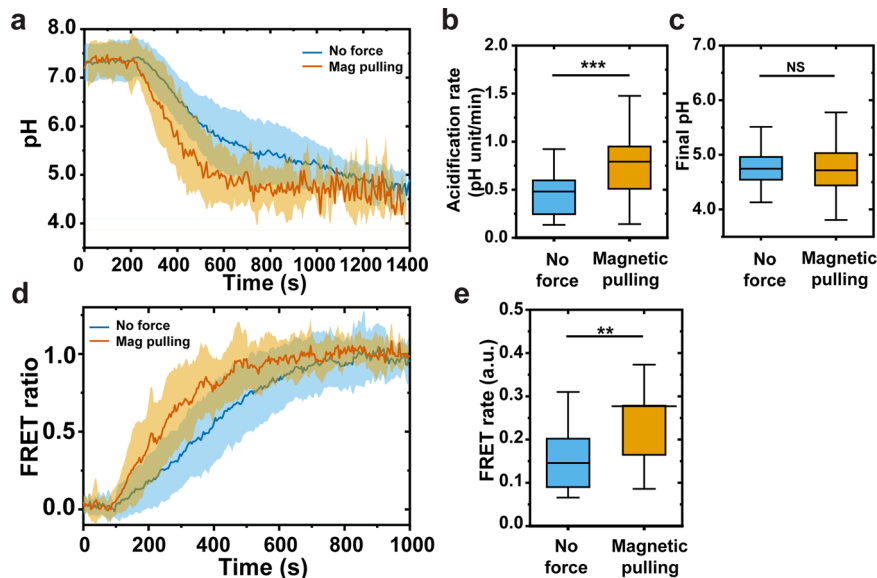


Fig. 5 Phagosome acidification and phagosome-lysosome fusion under magnetic pulling. **a** Line plots showing the average phagosome pH as a function of time with or without magnetic pulling as indicated. Each line plot is an average of 20 phagosomes. Shaded areas represent standard deviations. **b** Box graph showing the average acidification rate of phagosomes with or without magnetic pulling. The average acidification rate is 0.48 ± 0.34 pH unit/min without magnetic pulling ($N = 33$ phagosomes in 29 cells from 11 independent experiments) and 0.79 ± 0.54 pH unit/min with magnetic pulling ($N = 38$ phagosomes in 38 cells from 13 independent experiments). **c** Box graph showing the average final pH in different experiment conditions as indicated. The average final pH is 4.7 ± 0.3 without magnetic manipulation ($N = 33$) and 4.7 ± 0.4 with magnetic pulling ($N = 38$). **d** Line plots showing the average normalized FRET ratio as a function of time with or without magnetic pulling as indicated. The line curves are averaged from 20 individual phagosomes in each experimental condition. Shaded areas represent standard deviations. **e** Box graph showing the average normalized FRET rate in different experiment conditions as indicated. The average FRET rate is 0.15 ± 0.07 without magnetic manipulation ($N = 20$ phagosomes in 16 cells from 4 independent experiments) and 0.28 ± 0.21 with magnetic pulling ($N = 20$ phagosomes in 19 cells from 8 independent experiments). In **b**, **c**, and **e**, each box plot indicates the mean (horizontal line) and the interquartile range from 25% to 75% of the corresponding data set. Statistical significance is highlighted by p values (Mann-Whitney U Test) as follows: $**p < 0.01$, $***p < 0.001$, NS $p > 0.05$.

BSA-Alexa647-biotin (10 $\mu\text{g/ml}$) was used to load lysosomes. As shown in Fig. 5d and Supplementary Movies 1 and 2 the FRET signals from magnetically pulled phagosomes (average from $N = 20$ each) were noticeably more intense and increased more rapidly, indicating enhanced phagosome fusion with lysosomes. The FRET rate, which indicates the phagosome-lysosome fusion kinetic rate, is 0.28 ± 0.21 a.u. ($N = 20$) for phagosomes under magnetic pulling, in contrast to the average rate of 0.15 ± 0.07 a.u. without magnetic forces ($N = 20$) (Fig. 5e). To investigate whether the movement of phagosomes alone is sufficient to facilitate productive fusion with lysosomes, we next treated cells with nocodazole, which disrupts microtubule-based transport of both phagosomes and lysosomes. We then magnetically moved phagosomes the same way as in non-treated cells. Despite the fast movement of phagosomes under magnetic pulling forces, they exhibited minimal fusion with lysosomes and minimal acidification (Supplementary Fig. 28). This suggests that productive phagosome-lysosome fusion requires active transport of not only the phagosomes but also the lysosomes that they fuse with.

The magnetic tweezers results, taken together, demonstrate that faster transport of phagosomes on microtubules promotes their encounters with lysosomes, which leads to faster acidification. This explains why phagosome transport velocity positively correlates with phagosome-lysosome fusion kinetics and acidification rate.

Discussion

Phagosomes, even those from the same cells, show a substantial amount of variation from one another in their degradation and transport. The phagosome-to-phagosome variations have been demonstrated previously by the different amounts of degradative

enzymes transferred from lysosomes to phagosomes^{48–50} and of molecular motors recruited to phagosomes^{51–53}. Each phagosome functions as a separate degradative unit with its own distinct degradation kinetics^{10–12,49,54,55} and transport velocity^{2,56}. It was hypothesized that the biochemical state of a single phagosome could be influenced by many intracellular factors including signaling events in its surroundings⁵⁰. However, there is no known quantitative relationship between the seemingly stochastic rates of degradation of single phagosomes and their equally stochastic transport dynamics. In the current study, we report a single-phagosome imaging and manipulation toolset that allowed us to probe both degradative processes and dynamics of individual phagosomes. Multimodal particle sensors, called RotSensors, were engineered as phagosome probes to measure acidification within the lumen of an individual phagosome, the kinetics of that same phagosome's fusion with lysosomes, and its overall rotational and translational motion within the cell. The RotSensors were further combined with magnetic tweezers to perturb phagosome transport and observe the consequences for the maturation of single phagosomes. This integrated approach allowed us to demonstrate that the biochemical progression of degradative functions in individual phagosomes is coupled to and determined by the dynamics of their active transport.

By simultaneously tracking the transport dynamics and maturation of single phagosomes, we first determined that phagosomes that move faster centripetally fuse with lysosomes and acidify faster. While phagosome maturation is known to require microtubule-dependent transport^{19,21,35,52,53,57–59}, our results demonstrate that the seemingly stochastic rate of maturation of single phagosomes is positively correlated with their equally stochastic microtubule-based transport velocity. We showed that

phagosomes with higher centripetal motility exhibit much higher fusion rate with lysosomes. Because lysosomes are enriched in perinuclear region (Fig. 3a) and the perinuclear lysosomes are more acidic than those near cell periphery^{60,61}, it is plausible that active centripetal transport by molecular motors enhances the probability of physical collision between a phagosome and lysosomes, hence promoting phagosome maturation. Supporting this model, we showed that when phagosomes are accelerated centripetally toward nucleus under magnetic force, they speed up their fusion with lysosomes and their acidification. On the contrary, when phagosomes are prevented from moving towards the nucleus but instead magnetically held near the cell periphery, their acidification is disrupted, resulting in lower acidification and higher final pH. The centripetal transport of phagosomes leads to two possible consequences. First, it allows phagosomes to make physical contact and fuse with lysosomes, so faster-moving phagosomes have higher chance of fusion with lysosomes. Second, phagosomes after transport reach the perinuclear region where lysosomes tend to be more concentrated than near the cell periphery. These two factors are tightly coupled, as the subcellular location of phagosomes is largely determined by their transport dynamics. In fact, we observed that phagosomes that move faster also tend to be closer to the perinuclear region. These results demonstrate that the centripetal motility of phagosomes directly determines the kinetics of phagosome-lysosome fusion, and consequently the acidification kinetics. Centripetal transport of phagosomes effectively functions as a clock that determines the timing of the sequential biochemical activities during their maturation. Surprisingly, phagosome motility does not seem to influence their final pH. We further confirm that productive phagosome-lysosome fusion requires the microtubule-based transport of phagosomes as well as lysosomes. Once microtubules are disrupted, phagosomes fail to fuse with lysosomes or to acidify, even if phagosomes were moved magnetically. This observation agrees with previous studies showing that lysosome transport on microtubules is required for their fusion with phagosomes^{57,62}.

Our findings here opened doors to many interesting questions centered on the possible protein machineries that link the microtubule-based transport of phagosomes with their maturation kinetics. One molecule of interest is dynein. We reported previously that the “tug-of-war” between dynein and kinesin motors at microtubule intersections can lead to rotation of cargos that they carry⁶³. We observed here a positive correlation between the rotational velocity of phagosomes and their maturation rate (for both acidification and fusion with lysosomes). This strongly suggests that dynein might play a role, or multiple roles, in linking these two processes. It was shown previously that Rab7-RILP (Rab7-interacting lysosomal protein) complex helps recruit the dynein-dynactin motor protein complex to phagosomes^{33,64}, and the clustering of dynein generates extra force to mediate the rapid centripetal transport of phagosomes towards the perinuclear region⁵³. The phagosomal marker Rab7 can bridge phagosomes with dynein-dynactin, and also directly recruits the homotypic fusion and vacuole protein sorting complex and V-ATPase subunit V1G1, which are involved in membrane fusion and phagosome acidification^{65,66}. Beyond the molecular mechanisms, dynein may temporally influence phagosome maturation by controlling lysosome transport^{43,67} and by remodeling phagosome membranes^{43,64,67–69}. We showed that the active transport of lysosomes is important for the productive phagosome-lysosome fusion. Moreover, dynein can drive phagosome tubulation and therefore further promote fusion of phagosomes with lysosomes that reside on the same microtubules⁶⁴. These lysosome tubules could enable efficient phagosome-lysosome fusion, independent from the motor-driven

motility of phagosomes. Future work is warranted to disentangle the contributions from motor-driven transport and dynein-induced membrane tubulation in phagosome maturation. Besides dynein, there are other protein machineries that might link phagosome maturation kinetics with the transport dynamics. For instance, microtubule-associated proteins activate PI3K-Akt signaling⁷⁰ which can promote phagosome-lysosome fusion⁷¹.

In addition to studying phagosomes, we envision that the RotSensor toolset presented here could be further applied, with appropriate modifications, to studying intracellular pathogens and endosome maturation. Many pathogens, such as the bacterium *Legionella pneumophila*, hijack the phagosome-lysosome fusion process to evade immune clearance^{13–15}. Our study here was done with synthetic beads, which are far less complex than pathogens. Nevertheless, the results imply that intracellular pathogens might prolong their survival in host cells by disrupting the intracellular transport of phagosomes to slow down fusion with lysosomes and thus delay the degradation. This hypothesis can be tested in future studies where pathogen-extracted bio-particles or intact pathogens, instead of synthetic particles, can be used in the single-particle assays. Similarly, when smaller nanoparticles are used to replace the micron-sized beads in the single-particle assays, it will be possible to study the degradative function of endosomes that are smaller than phagosomes.

Methods

Materials. Carboxylate-modified yellow-green fluorescent polystyrene nanoparticles (diameter 100 nm), carboxylate-modified superparamagnetic Dynabeads (diameter 1 μ m), Trypan blue stain (0.4%), pentylamine-biotin, Alexa Fluor 568 NHS ester (succinimidyl ester), Alexa Fluor 647 NHS ester (succinimidyl ester), pHrodo iFL Red STP Ester, Streptavidin, LysoTracker Green DND-26, Alexa Fluor 405 goat anti-rabbit IgG (H+L), Alexa Fluor 488 anti-tubulin- α antibody, Alexa Fluor Plus 647 phalloidin, and DQ-green BSA were purchased from ThermoFisher (Waltham, MA). Immunoglobulin G from rabbit plasma, albumin from bovine serum (BSA), biotin N-hydroxysuccinimide ester (biotin-NHS), nocodazole, and lipopolysaccharides were purchased from Sigma-Aldrich (St. Louis, MO). Mono-disperse amine-modified silica particles (diameter 1.0 μ m) were purchased from Spherotech Inc. (Lake Forest, IL). SYLGARD™ 184 Silicone Elastomer kit was from Dow Corning (Midland, MI). 1-(3-Dimethylaminopropyl)-3-ethylcarbodiimide hydrochloride (EDC) was purchased from Alfa Aesar (Haverhill, MA). Nigericin sodium salt was purchased from Tocris Bioscience (Minneapolis, MN). Recombinant Murine IFN- γ was purchased from Peprotech (Rocky Hill, NJ). CF640R-amine was purchased from Biotium (Fremont, CA). RAW264.7 macrophage was purchased from ATCC (Manassas, VA). FuGENE HD transfection reagent was purchased from Promega (Madison, WI). RAW264.7 macrophages stably expressing EGFP-actin have been previously described⁴⁵. EGFP-LAMP1 was prepared following the reported protocol⁷². Ringer’s solution (pH = 7.3, 10 mM HEPES, 10 mM glucose, 155 mM NaCl, 2 mM NaH₂PO₄, 5 mM KCl, 2 mM CaCl₂, 1 mM MgCl₂) was used for live-cell imaging. Potassium-rich solution (135 mM KCl, 2 mM K₂HPO₄, 1.2 mM CaCl₂, 0.8 mM MgSO₄) was used for intracellular pH calibration. Acidic washing solution (135 mM KCl, 2 mM K₂HPO₄, 1.2 mM CaCl₂, 0.8 mM MgSO₄, 5 mM sodium citrate) at pH of 4.5 was used for particle washing in the EDC coupling step of the RotSensor fabrication. Artificial lysosome fluid (55 mM NaCl, 0.5 mM Na₂HPO₄, 0.26 mM trisodium citrate dihydrate, 0.79 mM glycine, 150 mM NaOH, 108 mM citric acid, 0.87 mM CaCl₂·2H₂O, 0.27 mM Na₂SO₄, 0.25 mM MgCl₂·6H₂O, 0.46 mM disodium tartrate, 1.6 mM sodium pyruvate) was prepared following a previously reported protocol⁷³ and used for washing particles during the protein conjugation step of the RotSensor fabrication.

Cell culture, pharmacological treatments, and transfection. Both RAW264.7 macrophage and stable cell line expressing EGFP-actin were cultured in Dulbecco’s Modified Eagle Medium (DMEM) complete medium supplemented with 10% fetal bovine serum, 100 units/ml penicillin, and 100 μ g/ml streptomycin at 37 °C and 5% CO₂. Resting macrophages were activated with a combination of 50 ng/ml LPS and 100 units/ml IFN- γ for 9 h prior to live cell imaging. Microtubule depolymerization was achieved by incubating cells with 10 μ M nocodazole for 1 h prior to imaging, and 10 μ M nocodazole was presented during live cell imaging. Transfection of RAW264.7 macrophage cells with LAMP1-GFP was performed according to manufacturer’s instructions. Briefly, 3 μ l FuGENE HD transfection reagent and 1000 ng of plasmid were mixed in 100 μ l DMEM and kept at room temperature for 15 min. After that, the mixture was added gently to cells and incubated with cells at 37 °C with 5% CO₂ for 18 h. Cells were washed three times with Ringer’s solution before live cell imaging.

Fluorescence labeling of streptavidin and bovine serum albumin (BSA). To prepare streptavidin-pHrodo Red conjugates (SAV-pHrodo Red), 0.7 mg of streptavidin, 60 µg of pHrodo Red STP Ester were mixed in 350 µl NaHCO₃ solution (100 mM, pH 8.2) for 3 h at room temperature. Free dyes were removed by centrifugal filtration using Amicon Ultra filters (30 K). To prepare streptavidin-CF640R conjugates (SAV-CF640), 0.7 mg of streptavidin, 80 µg of CF640R-amine, and 3 mg of EDC were mixed in 350 µl MES buffer (50 mM, pH 4.5) for 3 h at room temperature. Free dyes were removed by centrifugal filtration using Amicon Ultra filters (30 K). To prepare streptavidin-Alexa568 conjugates (SAV-Alexa568), 0.5 mg of streptavidin, 60 µg of Alexa Fluor 568 NHS ester were mixed in 235 µl NaHCO₃ solution (100 mM, pH 8.2) for 1 h at room temperature. Free dyes were removed by centrifugal filtration using Amicon Ultra filters (30 K). To prepare bovine serum albumin-Alexa647-biotin (BSA-Alexa647-biotin) conjugates, a mixture containing 2 mg/ml BSA and 188 µg/ml (molar ratio of 1:20) biotin-NHS in NaHCO₃ solution (100 mM, pH 8.2) was incubated at room temperature for 1 h. Unbound biotin-NHS was removed by centrifugal filtration using Amicon Ultra filters (30 K). After washing, a mixture containing 2 mg/ml BSA-biotin and 780 µg/ml Alexa Fluor 647 NHS ester in NaHCO₃ solution (100 mM, pH 8.2) was incubated at room temperature for 3 h. Free dyes were removed by centrifugal filtration using Amicon Ultra filters (30 K). The resulting BSA-Alexa647-biotin yielded dye: protein ratios of 1.2:1 on NanoDrop UV-Vis measurement (ThermoFisher, Waltham, MA). To prepare bovine serum albumin-Alexa647 (BSA-Alexa647) conjugates, a mixture containing 2 mg/ml BSA and 780 µg/ml Alexa Fluor 647 NHS ester in NaHCO₃ solution (100 mM, pH 8.2) was incubated at room temperature for 1 h. Free dyes were removed by centrifugal filtration using Amicon Ultra filters (30 K). The resulting BSA-Alexa647 yielded dye: protein ratios of 1.3:1 based on NanoDrop UV-Vis measurement (ThermoFisher, Waltham, MA).

Fabrication of Rotational Phagosome Sensors (RotSensors). RotSensors: Amine-modified non-fluorescent silica particles (1 µm) were incubated with 150 µg/ml biotin-NHS in NaHCO₃ solution (10 mM, pH 8.25) for 2 h at room temperature and then with 500 µg/ml of biotin-NHS for 30 min for the second round of biotinylation. After biotinylation, silica particles were washed in methanol and deionized water. The “snowman”-like design was introduced by covalently conjugating the carboxylate-modified yellow-green fluorescent nanoparticles (100 nm) to the biotinylated and amine-modified silica particles (1 µm) using EDC coupling. In brief, carboxylate-modified yellow-green fluorescent nanoparticles (100 nm) were mixed with the biotinylated and amine-modified silica particles (1 µm) at a molar ratio of 333:1 in phosphate buffer (10 mM, pH 7.0) containing 1.0 mg/ml EDC for 2 h at room temperature. After the EDC coupling, particles were washed with acidic washing solution and 1×PBS to remove the non-covalently bounded carboxylate-modified yellow-green fluorescent nanoparticles (100 nm). 20% of the particles were found to have the “snowman” shape with 1:1 coupling ratio of the biotinylated and amine-modified silica particles (1 µm) and the carboxylate-modified yellow-green fluorescent nanoparticles (100 nm).

pH-RotSensors: pH-RotSensors were fabricated by labeling RotSensors with SAV-pHrodo Red and SAV-CF640. RotSensors were incubated with 25 µg/ml of SAV-pHrodo Red, 2.5 µg/ml of SAV-CF640, 5 µg/ml of BSA, and 1 µg/ml of IgG in 1×PBS for 5 h at room temperature. Unbound proteins were rinsed off with artificial lysosome fluid and 1×PBS. The resulting pH-RotSensors were further opsonized with 30 µg/ml IgG in 1×PBS for additional 2 h before adding to cell samples.

FRET-RotSensors: FRET-RotSensors were fabricated by labeling RotSensors with SAV-Alexa 568. The RotSensors were incubated with 27.5 µg/ml of SAV-Alexa568, 5 µg/ml of BSA, and 1 µg/ml of IgG in 1×PBS for 5 h at room temperature. Unbound proteins were rinsed off with artificial lysosome solution and 1×PBS. The FRET-RotSensors were further opsonized with 30 µg/ml of IgG in 1×PBS for additional 2 h before adding to cell samples.

To confirm IgG adsorption on RotSensors, synthesized RotSensors were incubated for 30 min with 20 µg/ml IgG-Alexa Fluor 405 under gentle mixing. Excess antibodies were washed away by centrifugation and rinsing with 1×PBS three times. Epi fluorescence emissions at three wavelengths (ex: 402, 561, and 660 nm; em: 450, 586, and 680 nm) were acquired for imaging Alexa Fluor 405, pHrodo Red, and CF640R on RotSensors, respectively.

Fabrication of magnetically modulated phagosome sensors (MagSensors).

pH-MagSensors: The first step is the biotinylation of carboxylate-modified Dynabeads (1 µm). In brief, 10 µl of stock Dynabeads suspension (10 mg/ml) were added to 100 µl of MES buffer (50 mM, pH 6.2) containing 10 mg/ml EDC and 1 mM of biotin pentylamine. After 1-h incubation at room temperature, biotinylated Dynabeads (1 µm) were washed in 1×PBS to remove unbound biotin pentylamine. pH-MagSensors were fabricated by labeling biotinylated Dynabeads (1 µm) with SAV-pHrodo Red and SAV-CF640. Biotinylated Dynabeads were incubated with 50 µg/ml of SAV-pHrodo Red and 50 µg/ml of SAV-CF640 for 1 h at room temperature. The resulting pH-MagSensors were further opsonized with 1 mg/ml of IgG in 1×PBS for additional 1 h before adding to cell samples.

FRET-MagSensors: Biotinylated Dynabeads (1 µm) were prepared following the same procedure described above. FRET-MagSensors were fabricated by labeling biotinylated Dynabeads (1 µm) with SAV-Alexa568. Biotinylated Dynabeads were incubated with 27.5 µg/ml of SAV-Alexa568 for 1 h at room temperature. The

resulting FRET-MagSensors were further opsonized with 1 mg/ml of IgG in 1×PBS for additional 1 h before adding to cell samples.

Magnetic tweezers setup and force calibration. Magnetic tweezers were built on an inverted fluorescence microscope system (Nikon Eclipse Ti-U, Nikon, Tokyo, Japan), as shown in Supplementary Fig. 20. The setup mainly includes a solenoid and a power supply. The solenoid was assembled by inserting a high permeability HyMu-80 alloy rod (Carpenter Technology, Reading, PA) into an aluminum bobbin wrapped with 600 turns of copper coil⁷⁴ (Supplementary Fig. 20b). The tip of the rod has a diameter of ≈1 µm (Supplementary Fig. 20c). Position of the solenoid was controlled with a manual micromanipulator (Narishige NMN-21) to achieve independent control of its position in the *x*-, *y*-, and *z*-direction with a minimum graduation of 250 nm in the *x-y* plane and 1 µm in the *z*-direction. The current going through the solenoid was generated by a programmable power supply (Tekpower, Montclair, CA) with a maximum power output of 5 A.

Magnetic force was calibrated as a function of particle-to-tip distance by measuring the movements of Dynabeads (1 µm) in magnetic field using MATLAB algorithm⁷⁵. In brief, CF640R labeled Dynabeads (1 µm) were suspended in base solution of SYLGARD™ 184 Silicone Elastomer kit at a concentration of ≈3.0 × 10⁵ particles/ml. This low particle concentration was necessary to avoid particle aggregation and inter-particle magnetic inference⁷⁶. The base solution of SYLGARD™ 184 Silicone Elastomer kit, which has a high viscosity of 5.1 Pa s, was chosen to slow down particle movements to make particle tracking feasible. The initial positions of the solenoid tip and of the magnetic particles were imaged in bright field before time-lapse epi-fluorescence images of particles were acquired with an interval time of 0.2 s. Working current of the magnetic tweezers was 1.0 A in the calibration. The magnetic force $F(r)$ exerted on each magnetic particles at particle-to-tip distance r was converted from particle velocity values using Stokes' law:

$$F(r) = 3 \cdot \pi \cdot \eta \cdot d \cdot v, \quad (1)$$

where η is the viscosity of base solution of SYLGARD™ 184 Silicone Elastomer kit, d represents the diameter of particle, and v is the velocity of particle. The relationship between magnetic force $F(r)$ and particle-to-tip distance r was fitted using equation:

$$F(r) = \frac{F_0}{\left[\frac{r}{r_0} + \frac{1}{2}\right]C_F}, \quad (2)$$

where F_0 is a force constant with the unit of pN, r_0 is a distance constant with the unit of µm, C_F is unitless and $F_{(r_0)} = F_0^{74}$.

In the magnetic manipulation experiments, the magnetic tweezers tip was positioned as closely as possible to the glass coverslip on which cells were cultured. Due to the physical size of the magnetic solenoid tip, the axis of the solenoid rod was not exactly parallel to the *x-y* plane. Considering this, magnetic pulling in *z*-dimension is expected even though we didn't observe obvious particle movement along the *z*-axis. In this study, we only considered the projection of the 3D force into *x-y* plane.

Single-phagosome pH assay. RAW264.7 macrophage cells were seeded on glass coverslips at 2.0 × 10⁵ cells/ml in complete medium for 24 h and then activated with LPS and IFN-γ following the procedure described above. For all single-phagosome pH studies, the recognition of pH-Sensors (i.e., pH-RotSensor and pH-MagSensor) by macrophages was synchronized following a previously reported protocol⁷⁷. Briefly, cell samples were cooled on ice for 3 min to postpone phagocytosis. pH-Sensors were then added at a particle-to-cell ratio of ~5:1. Bindings of particles on macrophage were synchronized by centrifuging cell samples at 200 × g for 30 s. Live cell imaging was conducted in Ringer's solution at 37 °C on a Nikon Eclipse-Ti inverted microscope equipped with a 1.49 N.A. ×100 TIRF objective (Nikon, Tokyo, Japan) and an Andor iXon3 EMCCD camera (Andor Technology, Belfast, U.K.). Fluorescence emissions at three wavelengths (ex: 488, 561, and 660 nm; em: 515, 586, and 680 nm) were acquired for the time-lapse imaging. The acquisition rate was 2 s/frame. Single-phagosome pH assay in actin-GFP expressing RAW264.7 macrophages was conducted following the same procedure described above.

Single-phagosome FRET-fusion assay. RAW264.7 macrophage cells were seeded on glass coverslips at 2.0 × 10⁵ cells/ml in complete medium for 24 h and then activated with LPS and IFN-γ following the procedure described above. Loading of either BSA-Alexa647-biotin or BSA-Alexa647 into lysosome compartment was carried out following a previously reported pulse-chase protocol^{78–80}. In brief, RAW264.7 macrophage cells were incubated overnight in complete medium containing either BSA-Alexa647-biotin or BSA-Alexa647 at indicated concentration. 2 h prior to live cell imaging, cells were rinsed twice with complete medium. Labeled endocytic compartment was then chased at 37 °C for 2 h to ensure complete accumulation and fragmentation of fluorescently labeled BSA in lysosome compartments (Supplementary Figs. 12 and 13).

Synchronized internalization of FRET-Sensors (i.e., FRET-RotSensor and FRET-MagSensor) was conducted following the same procedure described above. Time-lapse epi-fluorescence images were acquired to record FRET emission

(FRET₀; ex/em 561/680 nm), donor emission (Alexa568_{em}; ex/em 561/586 nm), acceptor emission (Alexa647_{em}; ex/em 660/680 nm) and the emission from 100 nm yellow-green fluorescence particle (ex/em 488/515 nm). The acquisition rate was 4 s/frame.

The broad emission spectra of Alexa568 (donor) overlap partially with the acceptor emission channel (680 nm) and the broad excitation spectra of Alexa647 (acceptor) did overlap partially with donor excitation channel (561 nm). This resulted in two types of spectral cross-talks: (i) the detection of donor fluorophore (Alexa568) emission at acceptor emission channel (680 nm) under the donor excitation of 561 nm and (ii) the detection of acceptor fluorophore (Alexa647) emission at acceptor emission channel (680 nm) under the donor excitation of 561 nm in the absence of FRET effect. These two cross-talks, however, are constant throughout FRET-fusion assay, and could be deducted from the measured FRET emission (FRET₀) to obtain FRET-generated emission (FRET_{em}). Correction factors α and β for cross-talks were determined for each independent experiment based on: (1) the measured FRET emission and donor emission of Alexa568 streptavidin particles outside cells and (2) the measured FRET emission and acceptor emission of acceptor fluorophore (Alexa647) in cells without FRET-sensor. The FRET ratio is obtained as follows:

$$\text{FRET ratio} = \frac{\text{FRET}_{em}}{\text{AF568}_{em}} = \frac{\text{FRET}_0 - \alpha \times \text{AF568}_{em} - \beta \times \text{AF647}_{em}}{\text{AF568}_{em}}, \quad (3)$$

where FRET₀ is the measured FRET emission (ex/em 561/680 nm) before cross-talk correction, FRET_{em} is the FRET emission, AF568_{em} is the donor emission (ex/em 561/586 nm) and AF647_{em} is the acceptor emission (ex/em 660/680 nm). The FRET increase was gradual, not stepwise, because multiple dye-loaded lysosomes can simultaneously fuse with a single phagosome and the increment in FRET signal from a single phagosome-lysosome fusion is too small to be resolved.

For a thorough validation of the FRET assay, *in vitro* test of FRET-RotSensors was performed by mixing them with BSA-Alexa647 in 1×PBS (Supplementary Fig. 14). In this experiment, acceptor emission in the FRET channel could not be measured due to the excessive amount of free BSA-Alexa647 in solution. Instead, the percentage of donor quenching was quantified as an indirect indicator of FRET efficiency. Results show that the percentage of donor quenching, first increased linearly as a function of BSA-Alexa647 concentration in the lysosome loading solution ([BSA-Alexa647]_{loading}), but reached a plateau at [BSA-Alexa647]_{loading} > 200 µg/ml. This plateau indicates the maximum FRET efficiency which is determined by the amount of the donor fluorophore (Alexa568) available on RotSensors.

To optimize the loading concentration of BSA-Alexa647-biotin into lysosomes, [BSA-Alexa647-biotin]_{loading} from 2.5 µg/ml to 25 µg/ml was varied in experiment. Results indicate that higher [BSA-Alexa647-biotin]_{loading}, the more variation in the amount of BSA-Alexa647-biotin loaded into lysosomes between cells (Supplementary Fig. 15). As a result, the plateau level of FRET ratio had larger variations at [BSA-Alexa647-biotin]_{loading} > 10 µg/ml (Supplementary Fig. 17d). To estimate how the cell-to-cell variation affects the measurement of phagosome-lysosome fusion kinetics, the FRET ratio vs. time plot of each phagosome was normalized to its plateau level and then from the sigmoidal fitting of each FRET ratio plot, then the slope at half-response point t_0 as the kinetic rate of phagosome-lysosome fusion (referred to as FRET rate) was calculated (Fig. 2d and Supplementary Fig. 17e). In the FRET rate vs. [BSA-Alexa647-biotin]_{loading} plot (Supplementary Fig. 17f), the standard deviation of FRET rate between phagosomes increased significantly at [BSA-Alexa647-biotin]_{loading} > 10 µg/ml. All results suggest that an optimal range of [BSA-Alexa647-biotin]_{loading} for the FRET assay is ≤10 µg/ml. Therefore, 10 µg/ml, the highest concentration within this range, was used to improve the sensitivity of the FRET assay.

DQ-green BSA digestion assay. To estimate the fragmentation level of BSA-Alexa647-biotin chasing, we loaded DQ-green BSA into lysosome compartment following the same pulse-chase produced described above, and measured the dequenching kinetics of lysosomal DQ-green BSA as a function of time. A DQ-green BSA concentration at 50 µg/ml was used during pulse. After the overnight pulse, cells were rinsed three times with flour-free Ringer's solution and imaged using Epi-fluorescence microscope. The emission of DQ-green (ex/em 488/515 nm) was recorded every 5 min for 2 h.

Immunofluorescence imaging of actin and microtubules. RAW 264.7 macrophages were seeded and activated as described above. For immunostaining of α -tubulin and F-actin, cells were first washed with 1×PBS and fixed with 2% PFA at room temperature for 5 min. Next, they were permeabilized with 0.1% Triton X-100 for 5 min at room temperature, and blocked with 2% BSA for 1 h at room temperature. After the BSA blocking, cells were incubated with 2 µg/ml Alexa Fluor 488 anti-tubulin- α antibody and 2 µg/ml Alexa Fluor 647 phalloidin for 1 h at room temperature. Super-resolution structured illumination microscopy (SIM) images of the labeled cells were acquired using a DeltaVision OMX SR imaging system equipped with a Olympus Plan Apo 60×/1.42 PSF objective and a sCMOS camera.

Lysotracker labeling and imaging. RAW264.7 macrophages were seeded and activated as described above. After overnight incubation in complete medium containing 5 µg/ml BSA-Alexa647-biotin, the labeled endocytic compartments were chased at 37 °C for 1.5 h. Cells were then incubated with 50 nM LysoTracker

Green DND-26 at 37 °C for 30 min. After that, cells were rinsed twice with Ringer's solution to remove the free fluorophore and imaged using Re-scan Confocal Microscopy (RCM) equipped with a 1.49 N.A. ×100 TIRF objective and ORCA-fusion CMOS camera.

Trypan blue quenching assay. To distinguish the internalized RotSensors and MagSensors from those located outside of cells, trypan blue was added at the end of imaging to a final concentration of 4.6 µM followed by gentle mixing. Cell samples were imaged after 10 min of incubation. Fluorescence intensity of pHrodo Red (for pH-RotSensors and pH-MagSensors) and Alexa568 (for FRET-RotSensors and FRET-MagSensors) were used to differentiate internalized phagosomal sensors from extracellular ones.

Image registration. Image registration was done to correct the optical shift between different imaging channels. 100 nm TetraSpeck fluorescent particles (Ex/Em: 360/430 nm, 505/515 nm, 560/580 nm, and 660/680 nm) were adsorbed on poly-L-lysine-coated glass coverslips at a surface density of ≈0.10 bead/µm² and used as markers for image registration. After sequential imaging of the marker particles in three channels (Ex: 488, 561, and 660 nm), an affine transformation was applied to align particle localization maps from 488 and 660 nm channels (termed target images) to that from the 561 nm channel (reference image) using ImageJ plugin MultistackReg⁸¹. A global mapping matrix was obtained to record all the transformation steps and used to apply the same operations to all images.

Single-particle localization and intensity determination. The centroids of single particles in epi-fluorescence images were localized using a Gaussian-based localization algorithm in the ImageJ plugin Trackmate. To measure the emission of CF640R and pHrodo Red on pH-Sensors (i.e., pH-RotSensor and pH-MagSensor), pixel intensities within a diameter of 2 µm from the localized centroid of the particle were integrated and background-corrected using custom MATLAB algorithms. Same procedure was carried out for determining FRET₀, AF568_{em} and AF647_{em} in single-phagosome FRET-fusion assay. To determine the localization uncertainties, pH-RotSensors were immobilized on poly-L-lysine-coated glass coverslip and imaged for 200 consecutive frames in Ringer's solution. Localization uncertainty was defined as the standard deviation of the tracked particle positions in x - and y -coordinates. The localization uncertainties of the 1 µm pHrodo Red-coated particle and 100 nm yellow-green fluorescence nanoparticle were determined to be 20.6 ± 4.05 nm and 13.1 ± 2.32 nm, respectively (Supplementary Fig. 29).

Translational and rotational tracking analysis of RotSensors. The single particle tracking analysis was done as we previously reported^{26,82}. Briefly, translational velocity was determined from the centroid location of the 1 µm pHrodo Red- or SAV-Alexa568-coated particle (X_{red}, Y_{red}) as a function of time. For rotational tracking, a vector was drawn from the centroid of the 1 µm red fluorescent particle (X_{red}, Y_{red}) to that of the 100 nm yellow-green nanoparticle (X_{green}, Y_{green}) belonging to the same RotSensor. Orientation of the vector was obtained as the in-plane angle, φ , for the single RotSensor. The length of the vector was used to calculate the out-of-plane angle, θ , using the equation below:

$$\theta = \arcsin\left(\frac{d}{r}\right), \quad (4)$$

where d is the projection inter-particle distance between a pair of green and red dots in each given image, and r is the physical inter-particle distance. Because r varies slightly from one particle to another due to the size distribution, r was obtained as the maximal projected inter-particle distance d_{max} when a RotSensor samples all possible orientations and the d_{max} was larger than 550 nm. In cases when $d_{max} < 550$ nm, r was set to 550 nm. Two-dimensional rotational velocity was determined from the rotation matrix derived from φ and θ at consecutive frames. Using this method, φ can be measured within a full range (−180° to +180°), but there is ambiguity in measuring θ , because RotSensors oriented at a polar angle of θ or (180° − θ) are indistinguishable from one another when observed as a two-dimensional projection image. However, this ambiguity does not affect the measurements of $\Delta\theta$ and translational velocity in this study, because $\Delta\theta$ of phagosomes between consecutive image frames (2 s/frame) is expected to be < 90°, based on the result that phagosomes rotate an average $\Delta\varphi$ of 0.12 ± 0.16 rad (6.9° ± 9.2°) between consecutive frames (Supplementary Fig. 30). Therefore, only $\Delta\theta < 90^\circ$ was used in the tracking analysis for calculating rotational velocity of phagosomes.

Determination of active centripetal run. The directional transport of phagosomes was analyzed following a previously reported method with slight modification²². The centroid of the nucleus was obtained based on bright field image of the cell (Supplementary Fig. 31)^{56,58}. At each time point of a particle trajectory, the distances between the phagosome and the centroid of the nucleus was quantified (referred to as “distance-to-nucleus”) (Fig. 4b). The traveled distance of phagosome toward the nucleus was subdivided into segments with a length of 32 s. Each segment was categorized as either a segment of active run or as a segment of passive motion based on the traveled distance with regard to nucleus.

The distance threshold for active run was set to 0.5 μm , independent of the direction of motion whether it is towards the nucleus (centripetal) or towards the periphery (centrifugal)⁸³. Finally, segments of active runs were classified either as active centripetal run or as active centrifugal runs depending on the directionality of the transport.

Intracellular pH calibration. The intracellular pH calibration of pH-RotSensors and pH-MagSensors was done following a previously published protocol²⁸. Macrophages seeded on glass coverslips were pretreated with 10 μM concanamycin in Ringer's solution for 10 min before the addition of particles and then incubated at 37 °C for 10 min to promote particle phagocytosis. Cell medium was replaced with potassium-rich buffers at different pH values. All buffers contain 20 μM of nigericin, but different buffering agents: 5 mM acetic acid for pH 4.5, 5 mM MES for pH 5.5, and 5 mM HEPES for pH 6.5 and 7.3. The pH calibration was done from pH 7.3 to 4.5. For each pH, cells were rinsed twice with the correspondingly buffer and allowed to equilibrate for 5–10 min before image acquisition. Fluorescence emission of the pHrodo Red at 586 nm ($I_{\text{pHrodoRed}}$) and reference dye CF640R at 680 nm (I_{ref}) was obtained at various pH and background-corrected to obtain ratiometric pH calibration plots (Supplementary Fig. 3).

In live cell imaging, pH calibration was done for individual internalized pH-RotSensors and pH-MagSensors to eliminate the effect of particle-to-particle variation in their pH responses. By plotting $I_{\text{pHrodo}}/I_{\text{ref}}$ vs. time for single phagosomes, we notice that acidification process started with a standby period during which $I_{\text{pHrodo}}/I_{\text{ref}}$ ratio remains unchanged denoting that the phagosome pH remained equivalent to extracellular pH of 7.3 (Ringer's solution, pH = 7.3) before the initiation of phagosome acidification (Supplementary Fig. 32a, b). We further confirmed this by imaging phagosome acidification in cells expressing actin-GFP, in which intensity peak of actin-GFP pinpointed the time of particle internalization^{45,46} (Supplementary Fig. 32c–e). After live cell imaging, the same cell sample was incubated in pH 4.5 potassium-rich pH calibration buffer containing 20 μM of nigericin to obtain the ratiometric emission ($I_{\text{pHrodo}}/I_{\text{ref}}$) of the RotSensor at pH 4.5 (Supplementary Fig. 32a). In the final step of the calibration procedure, a linear function was generated based on the known $I_{\text{pHrodo}}/I_{\text{ref}}$ ratios at pH 4.5 and 7.3, and the result function was used to transform the fluorescence measurements of the RotSensor to luminal pH values (Supplementary Fig. 32b, f).

Wavelet transform analysis. A wavelet analysis algorithm reported by Chen et al. was used to distinguish active rotation from passive one. Both in-plane (θ) and out-of-plane (φ) displacement of a RotSensor was convoluted using the 1-dimensional Haar continuous time wavelet transform³⁴. The wavelet coefficients after the transformation were plotted as a function of time and for different widths of the wavelet function (Supplementary Fig. 9). The width of the wavelet function used here is the number of image frames and referred to as “scale”. Scale 10 was chosen as a universal threshold such that no active rotation of phagosomes was detected in cells that were treated with microtubule-disrupting drug nocodazole.

Determination of location of cell entry. The boundary of the cell was manually traced in ImageJ according to the fluorescence emission (ex/em 561/586 nm) of the cell in Ringer's solution containing trypan blue (Supplementary Fig. 31a). The boundary and the center of the nucleus were manually traced in ImageJ based on the bright field image of the given cell^{58,84} (Supplementary Fig. 31b).

Calculation of mean-square displacements (MSD). Time-resolved MSD shown in Fig. 4d was analyzed using custom MATLAB algorithms. Briefly, the MSD values of each single phagosome trajectory were calculated as a function of lag time δt based on the following equation:

$$\text{MSD}(\delta t) = \langle \Delta R(t)^2 \rangle = \langle (R(t + \delta t) - R(t))^2 \rangle \quad (5)$$

where $(R(t + \delta t) - R(t))$ is end-to-end displacement of an individual particle from the time point t to $t + \delta t$.

Transmission electron microscopy. Cell samples for TEM imaging were prepared based on a previously reported protocol with slight modification⁸². Particle sensors were incubated with cells for 50 min at 37 °C before trypsinization. After centrifugation, the cell pellet was fixed on ice for 1 h by using a mixture of 2.5% (w/v) glutaraldehyde and 1% (w/v) osmium tetroxide in 1×PBS buffer. Subsequently, the pellet was stained in 0.5% (w/v) uranyl acetate aqueous solution for 12 h on ice. Cell pellets were dehydrated sequentially in a series of ice-cold aqueous solutions containing 30% (v/v), 50%, 75%, 90%, 95%, and 100% ethanol for 5 min each. Dehydration in 100% (v/v) ethanol was repeated three times at room temperature. The dehydrated cell pellet was immersed sequentially in resin infiltration solutions that contain ethanol and Spurr's resin at various volume ratios (ethanol: resin, 2:1, 1:1, and 1:2) for 30 min each at room temperature. Cells were cured in 100% resin for 18 h at 65 °C prior to microtome sectioning. Sections were stained with 2% (w/v) uranyl acetate for 10 min before imaging. Samples were imaged with a JEOL

JEM-1010 Transmission Electron Microscope (Electron Microscopy Center, Indiana University).

Statistics and reproducibility. Statistical analyses of data were performed in OriginLab software. The results were analyzed by Student's t test or Mann-Whitney U test as described in figure legends. Statistical significance is highlighted by p values: * $p < 0.05$, ** $p < 0.01$, *** $p < 0.001$, **** $p < 0.0001$, NS $p > 0.05$. For all statistical analysis, data were collected from at least three individual replicates with exact sample numbers indicated in figure legends.

Reporting summary. Further information on research design is available in the Nature Research Reporting Summary linked to this article.

Data availability

All data needed to evaluate the conclusions in the paper are present in the paper and/or the Supplementary Materials. Additional data related to this paper may be requested from the authors. Supplementary Data for Fig. 1d–i Fig. 2c–f, Fig. 3b–e, Fig. 4c, d, and Fig. 5a, e and Supplementary Movie. 1 and 2 are available at Figshare⁸⁵.

Code availability

The MATLAB codes for rotational tracking of RotSensors are available upon request to corresponding author.

Received: 23 March 2022; Accepted: 12 September 2022;

Published online: 26 September 2022

References

- Harrison, R. E. & Grinstein, S. Phagocytosis and the microtubule cytoskeleton. *Biochem. Cell Biol.* **80**, 509–515 (2002).
- Al-Haddad, A. H. et al. Myosin VA bound to phagosomes binds to F-actin and delays microtubule-dependent motility. *Mol. Biol. Cell* **12**, 2742–2755 (2001).
- Araki, N. Role of microtubules and myosins in Fc gamma receptor-mediated phagocytosis. *Front. Biosci.* **11**, 1479–1490 (2006).
- Kelleher, J. F. & Titus, M. A. Intracellular motility: how can we all work together? *Curr. Biol.* **8**, R394–R397 (1998).
- Oberhofer, A. et al. Molecular underpinnings of cytoskeletal cross-talk. *Proc. Natl Acad. Sci. USA* **117**, 3944–3952 (2020).
- Steinberg, B., Huynh, K., Grinstein, S. Phagosomal Acidification: Measurement, Manipulation and Functional Consequences. Portland Press Ltd. (2007).
- Lennon-Duménil, A.-M. et al. Analysis of protease activity in live antigen-presenting cells shows regulation of the phagosomal proteolytic contents during dendritic cell activation. *J. Exp. Med.* **196**, 529–540 (2002).
- Rybicka, J. M., Balce, D. R., Chaudhuri, S., Allan, E. R. O. & Yates, R. M. Phagosomal proteolysis in dendritic cells is modulated by NADPH oxidase in a pH-independent manner. *Embo J.* **31**, 932–944 (2012).
- Henry, R. M., Hoppe, A. D., Joshi, N. & Swanson, J. A. The uniformity of phagosome maturation in macrophages. *J. Cell Biol.* **164**, 185–194 (2004).
- Podinovskaia, M. et al. Dynamic quantitative assays of phagosomal function. *Curr. Protoc. Immunol.* **102**, 14.34.11–14.34.14 (2013).
- Cheung, S., Greene, C. & Yates, R. M. Simultaneous analysis of multiple luminal parameters of individual phagosomes using high-content imaging. *Phagocytosis Phagosomes: Methods Protoc.* **1519**, 227–239 (2017).
- Balce, D. R., Rybicka, J. M., Greene, C. J., Ewanchuk, B. W. & Yates, R. M. Ligation of FcR alters phagosomal processing of protein via augmentation of NADPH oxidase activity. *Traffic* **17**, 786–802 (2016).
- Smith, L. M. & May, R. C. Mechanisms of microbial escape from phagocyte killing. *Biochem. Soc. Trans.* **41**, 475–490 (2013).
- Cossart P., Helenius A. Endocytosis of viruses and bacteria. *Cold Spring Harb. Perspect. Biol.* **6**, a016972 (2014).
- Kagan, J. C. & Roy, C. R. Legionella phagosomes intercept vesicular traffic from endoplasmic reticulum exit sites. *Nat. Cell Biol.* **4**, 945–954 (2002).
- Guerin, I. & de Chastellier, C. Disruption of the actin filament network affects delivery of endocytic contents marker to phagosomes with early endosome characteristics: the case of phagosomes with pathogenic mycobacteria. *Eur. J. Cell Biol.* **79**, 735–749 (2000).
- Gibbs, D., Kitamoto, J. & Williams, D. S. Abnormal phagocytosis by retinal pigmented epithelium that lacks myosin VIIa, the Usher syndrome 1B protein. *Proc. Natl Acad. Sci. USA* **100**, 6481–6486 (2003).

18. Arora, P. D., Manolson, M. F., Downey, G. P., Sodek, J. & McCulloch, C. A. A novel model system for characterization of phagosomal maturation, acidification, and intracellular collagen degradation in fibroblasts. *J. Biol. Chem.* **275**, 35432–35441 (2000).
19. Funato, K., Beron, W., Yang, C. Z., Mukhopadhyay, A. & Stahl, P. D. Reconstitution of phagosome-lysosome fusion in streptolysin O-permeabilized cells. *J. Biol. Chem.* **272**, 16147–16151 (1997).
20. Blocker, A. et al. Microtubule-associated protein-dependent binding of phagosomes to microtubules. *J. Biol. Chem.* **271**, 3803–3811 (1996).
21. Desjardins, M., Huber, L. A., Parton, R. G. & Griffiths, G. Biogenesis of phagolysosomes proceeds through a sequential series of interactions with the endocytic apparatus. *J. Cell Biol.* **124**, 677–688 (1994).
22. Keller, S., Berghoff, K. & Kress, H. Phagosomal transport depends strongly on phagosome size. *Sci. Rep.* **7**, 17068 (2017).
23. Jiang, M. et al. Microtubule motors transport phagosomes in the RPE, and lack of KLC1 leads to AMD-like pathogenesis. *J. Cell Biol.* **210**, 595–611 (2015).
24. Claus, V. et al. Lysosomal enzyme trafficking between phagosomes, endosomes, and lysosomes in J774 macrophages enrichment of cathepsin H in early endosomes. *J. Biol. Chem.* **273**, 9842–9851 (1998).
25. Savina, A. et al. NOX2 controls phagosomal pH to regulate antigen processing during crosspresentation by dendritic cells. *Cell* **126**, 205–218 (2006).
26. Yu, Y. Q., Gao, Y. & Yu, Y. “Waltz” of cell membrane-coated nanoparticles on lipid bilayers: tracking single particle rotation in ligand-receptor binding. *ACS Nano* **12**, 11871–11880 (2018).
27. Deriy, L. V. et al. Disease-causing mutations in the cystic fibrosis transmembrane conductance regulator determine the functional responses of alveolar macrophages. *J. Biol. Chem.* **284**, 35926–35938 (2009).
28. Nauffer, A. et al. pH of endophagosomes controls association of their membranes with Vps34 and PtdIns(3)P levels. *J. Cell Biol.* **217**, 329–346 (2018).
29. Nunes, P., Guido, D., Demaurex, N. Measuring phagosome pH by ratiometric fluorescence microscopy. *J. Vis. Exp.* **106**, e53402 (2015).
30. Canton, J., Khezri, R., Glogauer, M. & Grinstein, S. Contrasting phagosome pH regulation and maturation in human M1 and M2 macrophages. *Mol. Biol. Cell* **25**, 3330–3341 (2014).
31. Ogawa, M. et al. High sensitivity detection of cancer in vivo using a dual-controlled activation fluorescent imaging probe based on H-dimer formation and pH activation. *Mol. Biosyst.* **6**, 888–893 (2010).
32. Yates, R. M., Hermetter, A. & Russell, D. G. The kinetics of phagosome maturation as a function of phagosome/lysosome fusion and acquisition of hydrolytic activity. *Traffic* **6**, 413–420 (2005).
33. Gao, Y., Anthony, S. M., Yu, Y. Q., Yi, Y. & Yu, Y. Cargos rotate at microtubule intersections during intracellular trafficking. *Biophys. J.* **114**, 2900–2909 (2018).
34. Chen, K. J., Wang, B., Guan, J. & Granick, S. Diagnosing heterogeneous dynamics in single-molecule/particle trajectories with multiscale wavelets. *ACS Nano* **7**, 8634–8644 (2013).
35. Sun-Wada, G. H., Tabata, H., Kawamura, N., Aoyama, M. & Wada, Y. Direct recruitment of H⁺-ATPase from lysosomes for phagosomal acidification. *J. Cell Sci.* **122**, 2504–2513 (2009).
36. Pauwels, A. M., Trost, M., Beyaert, R. & Hoffmann, E. Patterns, receptors, and signals: regulation of phagosome maturation. *Trends Immunol.* **38**, 407–422 (2017).
37. Riazanski, V. et al. TRPC6 channel translocation into phagosomal membrane augments phagosomal function. *Proc. Natl Acad. Sci. USA* **112**, E6486–E6495 (2015).
38. Mcneil, P. L., Tanasugarn, L., Meigs, J. B. & Taylor, D. L. Acidification of phagosomes is initiated before lysosomal-enzyme activity is detected. *J. Cell Biol.* **97**, 692–702 (1983).
39. Yates, R. M. & Russell, D. G. Real-time spectrofluorometric assays for the luminal environment of the maturing phagosome. *Methods Mol. Biol.* **445**, 311–325 (2008).
40. Duvvuri, M. & Krise, J. P. A novel assay reveals that weakly basic model compounds concentrate in lysosomes to an extent greater than pH-partitioning theory would predict. *Mol. Pharm.* **2**, 440–448 (2005).
41. Fahrner, J., Funk, J., Lillich, M. & Barth, H. Internalization of biotinylated compounds into cancer cells is promoted by a molecular Trojan horse based upon core streptavidin and clostridial C2 toxin. *N.-S Arch. Pharm.* **383**, 263–273 (2011).
42. Horn, M. A., Heinstein, P. F. & Low, P. S. Characterization of parameters influencing receptor-mediated endocytosis in cultured soybean cells. *Plant Physiol.* **98**, 673–679 (1992).
43. Pu, J., Guardia, C. M., Keren-Kaplan, T. & Bonifacino, J. S. Mechanisms and functions of lysosome positioning. *J. Cell Sci.* **129**, 4329–4339 (2016).
44. Jiang, C., Lionberger, T. A., Wiener, D. M. & Meyhofer, E. Electromagnetic tweezers with independent force and torque control. *Rev. Sci. Instrum.* **87**, 084304 (2016).
45. Scott, C. C. et al. Phosphatidylinositol-4,5-bisphosphate hydrolysis directs actin remodeling during phagocytosis. *J. Cell Biol.* **169**, 139–149 (2005).
46. Huang, N. N. et al. Canonical and noncanonical g-protein signaling helps coordinate actin dynamics to promote macrophage phagocytosis of zymosan. *Mol. Cell Biol.* **34**, 4186–4199 (2014).
47. Hendricks, A. G., Holzbaur, E. L. & Goldman, Y. E. Force measurements on cargoes in living cells reveal collective dynamics of microtubule motors. *Proc. Natl Acad. Sci. USA* **109**, 18447–18452 (2012).
48. Gotthardt, D. et al. High-resolution dissection of phagosome maturation reveals distinct membrane trafficking phases. *Mol. Biol. Cell* **13**, 3508–3520 (2002).
49. Podinovskaia, M., Lee, W., Caldwell, S. & Russell, D. G. Infection of macrophages with *Mycobacterium tuberculosis* induces global modifications to phagosomal function. *Cell Microbiol.* **15**, 843–859 (2013).
50. Griffiths, G. On phagosome individuality and membrane signalling networks. *Trends Cell Biol.* **14**, 343–351 (2004).
51. Diakonova, M., Bokoch, G. & Swanson, J. A. Dynamics of cytoskeletal proteins during Fc gamma receptor-mediated phagocytosis in macrophages. *Mol. Biol. Cell* **13**, 402–411 (2002).
52. Blocker, A. et al. Molecular requirements for bi-directional movement of phagosomes along microtubules. *J. Cell Biol.* **137**, 113–129 (1997).
53. Rai, A. et al. Dynein clusters into lipid microdomains on phagosomes to drive rapid transport toward lysosomes. *Cell* **164**, 722–734 (2016).
54. Yu, Y. Q., Jiao, M. C., Zhang, Z. H. & Yu, Y. Single-phagosome imaging reveals that homotypic fusion impairs phagosome degradative function. *Biophys. J.* **121**, 459–469 (2022).
55. Jiao, M., Li, W., Yu, Y., Yu, Y. Anisotropic presentation of ligands on cargoes modulates degradative function of phagosomes. *Biophys. Rep.* **2**, 100041 (2022).
56. Le-Bury, G., Deschamps, C., Dumas, A., Niedergang, F. Phagosome migration and velocity measured in live primary human macrophages infected with HIV-1. *J. Vis. Exp.* **115**, 54568 (2016).
57. Huynh, K. K. et al. LAMP proteins are required for fusion of lysosomes with phagosomes. *EMBO J.* **26**, 313–324 (2007).
58. Dumas, A. et al. The HIV-1 protein Vpr impairs phagosome maturation by controlling microtubule-dependent trafficking. *J. Cell Biol.* **211**, 359–372 (2015).
59. Rai, A. K., Rai, A., Ramaiya, A. J., Jha, R. & Mallik, R. Molecular adaptations allow dynein to generate large collective forces inside cells. *Cell* **152**, 172–182 (2013).
60. Gowrishankar, S. et al. Massive accumulation of luminal protease-deficient axonal lysosomes at Alzheimer’s disease amyloid plaques. *Proc. Natl Acad. Sci. USA* **112**, E3699–E3708 (2015).
61. Johnson, D. E., Ostrowski, P., Jaumouille, V. & Grinstein, S. The position of lysosomes within the cell determines their luminal pH. *J. Cell Biol.* **212**, 677–692 (2016).
62. Blocker, A., Griffiths, G., Olivo, J. C., Hyman, A. A. & Severin, F. F. A role for microtubule dynamics in phagosome movement. *J. Cell Sci.* **111**, 303–312 (1998).
63. Gao, Y. et al. Single-janus rod tracking reveals the “Rock-and-Roll” of endosomes in living cells. *Langmuir* **34**, 1151–1158 (2018).
64. Harrison, R. E., Bucci, C., Vieira, O. V., Schroer, T. A. & Grinstein, S. Phagosomes fuse with late endosomes and/or lysosomes by extension of membrane protrusions along microtubules: role of Rab7 and RILP. *Mol. Cell Biol.* **23**, 6494–6506 (2003).
65. Balderhaar, H. J. K. & Ungermann, C. CORVET and HOPS tethering complexes—coordinators of endosome and lysosome fusion. *J. Cell Sci.* **126**, 1307–1316 (2013).
66. Kissing, S. et al. Vacuolar ATPase in phagosome-lysosome fusion. *J. Biol. Chem.* **290**, 14166–14180 (2015).
67. Yang, Z. F. & Klionsky, D. J. Mammalian autophagy: core molecular machinery and signaling regulation. *Curr. Opin. Cell Biol.* **22**, 124–131 (2010).
68. Li, X. R. et al. A molecular mechanism to regulate lysosome motility for lysosome positioning and tubulation. *Nat. Cell Biol.* **18**, 404 (2016).
69. Suresh, B. et al. Tubular lysosomes harbor active ion gradients and poise macrophages for phagocytosis. *Proc. Natl Acad. Sci. USA* **118**, e2113174118 (2021).
70. Batrouni, A. G. & Baskin, J. M. A. MAP for PI3K activation on endosomes. *Nat. Cell Biol.* **22**, 1292–1294 (2020).
71. Rajaram, M. V. S. et al. Akt and SHIP modulate francisella escape from the phagosome and induction of the Fas-mediated death pathway. *Plos One* **4**, e7919 (2009).
72. Minin, A. A. et al. Regulation of mitochondria distribution by RhoA and formins. *J. Cell Sci.* **119**, 659–670 (2006).
73. Pelfrene, A., Cave, M. R., Wragg, J., Douay, F. In vitro investigations of human bioaccessibility from reference materials using simulated lung fluids. *Int. J. Environ. Res. Public Health* **14**, 112 (2017).

74. Zahn, C. et al. Measurement of the magnetic moment of single Magnetospirillum gryphiswaldense cells by magnetic tweezers. *Sci. Rep.* **7**, 3558 (2017).
75. Parthasarathy, R. Rapid, accurate particle tracking by calculation of radial symmetry centers. *Nat. Methods* **9**, 724–U291 (2012).
76. Etoc, F. et al. Subcellular control of Rac-GTPase signalling by magnetogenetic manipulation inside living cells. *Nat. Nanotechnol.* **8**, 193–198 (2013).
77. FitzGerald, L. I. & Johnston, A. P. R. It's what's on the inside that counts: techniques for investigating the uptake and recycling of nanoparticles and proteins in cells. *J. Colloid Int. Sci.* **587**, 64–78 (2021).
78. Jeschke, A. & Haas, A. Sequential actions of phosphatidylinositol phosphates regulate phagosome-lysosome fusion. *Mol. Biol. Cell* **29**, 452–465 (2018).
79. Jeschke, A. et al. Phosphatidylinositol 4-phosphate and phosphatidylinositol 3-phosphate regulate phagolysosome biogenesis. *Proc. Natl Acad. Sci. USA* **112**, 4636–4641 (2015).
80. Becken, U., Jeschke, A., Veltman, K. & Haas, A. Cell-free fusion of bacteria-containing phagosomes with endocytic compartments. *Proc. Natl Acad. Sci. USA* **107**, 20726–20731 (2010).
81. Micheva, K. D., O'Rourke, N., Busse, B. & Smith, S. J. Array tomography: semiautomated image alignment. *Cold Spring Harb. Protoc.* **2010**, pdb prot5527 (2010).
82. Sanchez, L., Yi, Y. & Yu, Y. Effect of partial PEGylation on particle uptake by macrophages. *Nanoscale* **9**, 288–297 (2017).
83. Gross, S. P. et al. Interactions and regulation of molecular motors in Xenopus melanophores. *J. Cell Biol.* **156**, 855–865 (2002).
84. Ba, Q. L., Raghavan, G., Kiselyov, K. & Yang, G. Whole-cell scale dynamic organization of lysosomes revealed by spatial statistical analysis. *Cell Rep.* **23**, 3591–3606 (2018).
85. Zhang, Z., Yu, Y., Walpole, G. F. W., Yu, Y. Kinetics of phagosome maturation is coupled to their intracellular motility. *figshare* (2022).

Acknowledgements

We thank Prof. Sergio Grinstein at University of Toronto for his helpful discussion. We thank Mr. Andy Alexander at the Electronic Instrument Services of Indiana University for assistance with the setup of magnetic tweezers. We thank Dr. Barry Stein at the IUB Electron Microscopy Imaging Center, Dr. Jim Power at the IUB Light Microscopy Imaging Center (LMIC), Dr. Yi Yi at the Nanoscale Characterization Center for assistance with instrument use. The development of single-particle rotational tracking method was supported by the National Science Foundation, Division of Chemical, Bioengineering, Environmental, and Transport Systems under Award No. 1554078. All other research reported in this publication was supported by the National Institute of General Medical Sciences of the NIH under Award No. R35GM124918 (Y.Y.). G.F.W.W. is supported by a Vanier Canada Graduate Scholarship (CIHR). The content is solely the

responsibility of the authors and does not necessarily represent the official views of the NIH.

Author contributions

Y.-q.Y., Z.Z., and Y.Y. designed research; Y.-q.Y. and Z.Z. performed research and analyzed data; G.F. W.W. contributed critical reagents; Y.-q.Y., Z.Z., and Y.Y. wrote the paper and G.F.W.W. provided critical discussion.

Competing interests

The authors declare no competing interests.

Additional information

Supplementary information The online version contains supplementary material available at <https://doi.org/10.1038/s42003-022-03988-4>.

Correspondence and requests for materials should be addressed to Yan Yu.

Peer review information *Communications Biology* thanks the anonymous reviewers for their contribution to the peer review of this work. Primary Handling Editor: Manuel Breuer.

Reprints and permission information is available at <http://www.nature.com/reprints>

Publisher's note Springer Nature remains neutral with regard to jurisdictional claims in published maps and institutional affiliations.



Open Access This article is licensed under a Creative Commons Attribution 4.0 International License, which permits use, sharing, adaptation, distribution and reproduction in any medium or format, as long as you give appropriate credit to the original author(s) and the source, provide a link to the Creative Commons license, and indicate if changes were made. The images or other third party material in this article are included in the article's Creative Commons license, unless indicated otherwise in a credit line to the material. If material is not included in the article's Creative Commons license and your intended use is not permitted by statutory regulation or exceeds the permitted use, you will need to obtain permission directly from the copyright holder. To view a copy of this license, visit <http://creativecommons.org/licenses/by/4.0/>.

© The Author(s) 2022